Validation of martian meteorological data assimilation for MGS/TES using radio occultation measurements

Validation of Martian meteorological data assimilation for MGS/TES using radio occultation measurements

L. Montabone[1,2], S. R. Lewis[3], P. L. Read[1], and D. P. Hinson[4]

Icarus **185,** 113–132, doi:10.1016/j.icarus.2006.07.012, November 2006

[1]Atmospheric, Oceanic and Planetary Physics, Department of Physics, Oxford University, Parks Road, Oxford OX1 3PU, United Kingdom

[2]Laboratoire de Mètèorologie Dynamique du CNRS, Université Paris 6, Tour 45-55, 3ème étage, 4, place Jussieu, 75252 Paris Cedex 05, France

[3]Department of Physics & Astronomy, The Open University, Walton Hall, Milton Keynes MK7 6AA, United Kingdom

[4]Department of Electrical Engineering, Stanford University, 350 Serra Mall, Stanford, Ca 94305, USA

Abstract

We describe an assimilation of thermal profiles below about 40 km altitude and total dust opacities into a general circulation model (GCM) of the Martian atmosphere. The data were provided by the Thermal Emission Spectrometer (TES) on board the Mars Global Surveyor (MGS) spacecraft. The results of the assimilation are verified against an independent source of contemporaneous data represented by radio occultation measurements with an ultra-stable radio oscillator, also aboard MGS. This paper describes a comparison between temperature profiles retrieved by the radio occultation experiments and the corresponding profiles given by both an independent, carefully tuned GCM simulation and by an assimilation of TES observations performed over the period of time from middle, northern summer in Martian year 24, corresponding to May 1999, until late, northern

spring in Martian year 27, corresponding to August 2004. This study shows that the assimilation of TES measurements improves the overall agreement between radio occultation observations and the GCM analysis, in particular below 20 km altitude, where the radio occultation measurements are known to be most accurate. Discrepancies still remain, mostly during the global dust storm of year 2001 and at latitudes around 60°N in northern winter-early spring. These are the periods of time and locations, however, for which discrepancies between TES and radio occultation profiles are also shown to be the largest. Finally, a further direct validation is performed, comparing stationary waves at selected latitudes and time of year. Apart from biases at high latitudes in winter time, data assimilation is able to represent the correct wave behaviour, which is one major objective for Martian assimilation.

KEY WORDS: Mars, atmosphere; Data reduction techniques; Radio observations

1 Introduction

The Mars Global Surveyor spacecraft (MGS) has been in orbit around Mars since 1997, and during its mapping phase, starting in February 1999, has produced a synoptic dataset of almost three complete Martian years of atmospheric temperature, dust opacity measurements, water vapour and water ice observations below about 40 km altitude, using the Thermal Emission Spectrometer (TES) in the nadir viewing mode (Conrath et al., 2000; Smith et al., 2000, 2001; Smith, 2004). Since the end of August 2004, TES has been switched off, owing to the malfunction of the second of its two calibration lamps. The first lamp had already failed during MGS aerobraking.

Such an extensive atmospheric dataset, with a well sampled spatial and temporal coverage given by the 2-hour mapping phase polar orbit, presents a unique opportunity for the application of data assimilation techniques to a planetary atmosphere. The latter have already been suggested as an effective tool with which to analyse spacecraft observations of the Martian atmosphere, in the same way as they are implemented for operational weather forecasts on the Earth (Banfield et al., 1995; Lewis and Read, 1995; Lewis et al., 1996, 1997; Kass and Ingersoll, 1997; Houben, 1999; Zhang et al., 2001). Data assimilation aims to provide a complete, balanced, four-dimensional analysis

of observations for all atmospheric variables, including those for which no direct measurements are available, such as wind and surface pressure.

This technique has been succesfully adapted to the case of Mars by Lewis et al. (2005) to analyse some aspects of the zonal-mean state of the atmosphere, of the transient wave behaviour and of the Noachis dust storm in late 1997, by using TES observations made during the aerobraking phase of MGS, a time when the orbital period was reduced from 45 to 24 hours over the space of about 100 orbits. This configuration was far from optimal for assimilation, however, in particular because the period between orbits is significant compared both to the radiative timescale of 1-2 days in the lower Martian atmosphere and the typical periods of transient waves on Mars, which are around 2-10 days. Nevertheless, it has been an important initial test on another planet of an assimilation procedure based on the Analysis Correction scheme (Lorenc et al., 1991) with real, but sparse data, during a meteorologically interesting period on Mars (northern autumn).

A substantial body of data is now available from the scientific mapping phase of MGS, and assimilation of thermal profiles and total dust opacities retrieved from TES spectra in the nadir viewing mode has been performed to construct a seasonally-evolving, global picture of the Martian atmosphere. Assimilation of TES nadir retrievals into the Oxford version of the European Mars General Circulation Model (MGCM, Forget et al., 1999) has been carried out for a period of almost three complete Martian years, from middle (northern hemisphere) summer in the first year of the MGS mapping phase (Martian Year 24[1]) until late (northern hemisphere) spring in the fourth year (MY 27).

This extensive dataset is now being used for scientific studies such as the inter-annual variability of dust storms (Montabone et al., 2005) and the atmospheric thermal tides (Lewis and Barker, 2005). It is therefore important to validate the assimilated results, preferably against an independent and simultaneous source of observations. For the latter purpose, we use the temperature profiles retrieved from the radio occultation measurements made with the ultra-stable radio oscillator on board MGS (Hinson et al., 1999, 2001), acquired during approximately the same period of time as the assimilated TES profiles, although not at exactly the same locations and local

[1]In this convention, Martian year 1 begins at $L_s = 0$ on 11 April 1955; MY 24 begins on 14 July 1998. Clancy et al. (2000) propose this nomenclature as the new period of careful and 'unified' observations on Mars which begins after the observations of the global dust storm in 1956.

times.

This paper describes the results of this comparison with radio occultation profiles together with a comparison with thermal profiles provided by an independent, free-running MGCM simulation (control simulation). The objectives of this study are: (1) to perform a validation of the assimilation which gives confidence for its scientific use; (2) to provide an intercomparison of different datasets (MGS/TES, MGS/Radio Occultation, assimilation and control simulation), which contain observations distributed at different locations and times, in a consistent way; (3) to test the accuracy of the Martian GCM and to show how the assimilation technique can be extremely useful for detecting possible weaknesses and for refining the atmospheric model; and (4) to provide some initial result on stationary waves in the assimilated dataset and to compare them directly to the results obtained by Hinson et al. (2003, 2004) in the radio occultation dataset.

Section 2 outlines improvements in the GCM and the assimilation procedure made with respect to the previous work by Lewis et al. (2005). Section 3 describes briefly the radio occultation dataset used for the comparisons while section 4 deals with the comparison of the temperature profiles provided by the assimilation and the free-running MGCM with the radio occultation profiles. Section 5 analyses in detail the discrepancies found during the global dust storm of MY 25 and at high northern latitudes. Section 6 is devoted to the comparison of stationary waves with the results from radio occultations. Conclusions are drawn in section 7.

2 Mars General Circulation Model and Data Assimilation

The atmospheric model used in this study is the semi-spectral (Oxford) version of the Mars General Circulation Model, essentially as described in Forget et al. (1999) and in Lewis et al. (2005). The only difference here is that this study employed a prescribed dust scenario for the independent control simulation, based on MGS background dust observations (Smith et al., 2000), but with no individual dust storms modeled. This was originally designed as a default prescribed dust scenario for the European Mars Climate Database, an earlier version of which is described in Lewis et al. (1999). Fig. 1 shows the main parameters for this scenario: the total visible optical depth, τ, and

the height of the "top" of the dust layer, z_{max}. These are applied to the following equation which is used to describe the vertical distribution of the dust at a given latitude and time in terms of volume mixing ratio (cf. Forget et al., 1999):

$$q = q_0 \exp\left\{a\left[1 - (p_0/p)^{(b/z_{max})}\right]\right\}, \quad (1)$$

for pressure $p \leq p_0$, where p_0 is taken to be $p_0 = 700$ Pa, and with $q = q_0$ for $p > p_0$. q_0 is calculated to give the total optical depth shown in Fig. 1a for each areocentric longitude and latitude, and a and b are free parameters with values $a = 0.007$, $b = 70$ km. z_{max} varies with areocentric longitude L_s and latitude ϕ according to the equation:

$$\begin{aligned} z_{max} &= 60 + 18\sin(L_s - 160^\circ) - \sin^4\phi[32 + 18\sin(L_s - 160^\circ) \\ &\quad -8\sin(L_s - 160^\circ)\sin\phi]. \end{aligned} \quad (2)$$

This dust distribution gives a good statistical agreement with both radio occultation profiles and TES retrievals from MGS (Forget et al., 2001) and is thus taken as the best prescribed scenario for an independent control experiment in this study. From the point of view of the assimilation, the prescribed scenario in Fig. 1a is of little consequence to the results shown, since total dust opacities are directly assimilated. It is only used as the initial state for the assimilation until the first dust observations become available at a given longitude and latitude. On the other hand, since the nadir TES observations contain no information about dust distribution within the atmospheric column, Eq. 1 is still used to describe the vertical variation of dust with an updated q_0 at each location, as explained below.

— Figure 1 —

The data assimilation is conducted using a modified form of the sequential Analysis Correction scheme (Lorenc et al., 1991) with parameters tuned for the specific case of Mars. Details of the technique are summarized by Lewis et al. (2005). We only mention here that it combines information from both present and past observations of TES thermal profiles and dust optical depth, using the GCM to produce a time-evolving analysis of the atmospheric state. Observations are repeatedly introduced to the model spread over a six hour time window and with an empirically-determined horizontal correlation scale ($\sim 340-540$ km), both weighted towards the time and location at which each measurement is valid, in order to adjust the large scale and slowly-varying

components of the atmospheric flow. In the vertical, TES temperatures are assimilated in the form of layer thicknesses between pressure levels spaced one scale height apart in the lower atmosphere, to avoid artificially smoothing small-scale structures present in the model, which would not be seen in the nadir retrievals.

Diagnostic variables are typically recorded 12 times per sol, both in Fourier space (spectral resolution is T31, corresponding to a spectral truncation at wave number 31, or to 96×48 horizontal grid points) and on a regular physical grid of 72×36 points in longitude and latitude, with 25 vertical levels in σ coordinates, extending up to approximately 100 km altitude (the highest three layers act as sponge layers, to damp vertical propagating waves).

This study involves assimilation of thermal profiles and total dust opacities which are retrieved from nadir soundings of the Martian atmosphere, below about 40 km altitude, obtained by TES aboard MGS during the scientific mapping phase (see Conrath et al., 2000; Smith et al., 2000, for details of the retrieval technique). Note that the retrieved dust opacities from TES are in the infrared (wavelength around 1075 cm^{-1}), whereas the GCM radiation scheme computes dust heating rates based on a mean visible opacity. Total dust opacities have therefore been converted from the infrared to a mean visible value by multiplying by a factor of 2.0 (Clancy et al., 1995, 2003), although there is considerable uncertainty in the size and variability of this factor (Martin, 1986). Tests on different values of the conversion factor within the range 1.5–2.5, however, did not show significant differences in simulated temperature fields or climatology, as the assimilation of temperatures has a stronger impact on the model than the assimilation of dust opacities, at least under moderate dust conditions and when temperature data are plentiful (see Lewis and Read, 1995). See also section 5.1 for further details.

Since only total column dust opacities can be retrieved from nadir soundings, as mentioned above, the vertical distribution of the dust has to be prescribed, as in eq. (1), which assumes values of a, b and z_{max} as above. In this case q_0 is calculated to give the assimilated total optical depth in the visible at the appropriate latitude, longitude and time at the reference pressure of 700 Pa.

Figure 2 shows the period of time covered by MGS/TES data, for which assimilation has been performed to date. It begins at areocentric longitude $L_S = 141^\circ$ (late summer) of MY 24, which corresponds to May 1999, and ends at $L_S = 73^\circ$ (late spring) of MY 27, which corresponds to August 2004,

thus spanning almost three complete Martian years.

— Figure 2 —

In Fig. 2 we also plot, as a reference, the number of temperature and dust observations which have actually been assimilated after having passed a series of quality control checks. This quality control procedure has been detailed by Lewis et al. (2005), but in this study we have introduced a further restriction on TES thermal retrievals. Only temperatures above the condensation temperature for CO_2 ice at the corresponding pressure have been assimilated. The reason for this is the large discrepancy in the amount of CO_2 ice deposited at the poles during the winter seasons which arises in the results from the assimilation compared to the control simulation, if this restriction is not applied. This is due to an abnormally large amount of CO_2 condensation in the assimilation, which reflects either a lack of detailed and accurate representation in the model of the CO_2 physical processes in the polar regions, or a bias in the data. The effect of this abnormal condensation is that the surface pressure varies seasonally much more in the assimilation than in the control simulation. Moreover, the assimilation without restricting CO_2 condensation does not agree with previous comparisons with surface pressures measured by the Viking and Pathfinder landers. Our choice to disregard temperatures below the condensation temperature relies on two considerations. First, errors in the absolute radiometric calibration of TES affect the retrievals of temperature most strongly under cold atmospheric and surface conditions (Conrath et al., 2000), which makes supersaturated values of temperature less reliable. Second, the polar $mathrmCO_2$ condensation-sublimation scheme in the MGCM was tuned to reproduce measurements of surface pressure made by the two Viking landers. Thus the results from the assimilation are expected to be consistent with this tuning. Accordingly, it has found that if the above restriction on the assimilated temperatures is applied, the yearly variation of surface pressure matches the one of the control simulation.

At the time of the writing of this paper, there is uncertainty in the degree of supersaturation apparently seen in the TES temperature retrievals. Radio occultation thermal profiles, for instance, virtually never show supersaturation by more than 2 K, the amount required for heterogeneous nucleation (Hinson, 2006). The group involved in TES retrievals at the Goddard Space Flight Center (USA) also announced recently the release of a new set of

retrieved temperature profiles which are up to 10 K warmer in the winter polar region than in the earlier dataset (Smith, M. D., personal communication). The present study supports the idea that the previous release of TES retrieved temperature profiles was significantly cold-biased in polar regions. Future assimilation experiments will certainly include these corrections. It is desirable, however, that a more accurate representation of CO_2 processes in the polar region is implemented in the model, which will be an aim of future work.

3 Radio Occultation Measurements

Results from the control simulation and the data assimilation were compared and verified by using thermal profiles retrieved from the radio occultation soundings of the neutral atmosphere. Radio occultation measurements use the temperature-controlled "ultrastable" oscillator (USO) aboard MGS to send a microwave signal through the atmosphere at two points in the MGS polar orbit, the so-called "occultation entry" and "occultation exit" (Hinson et al., 1999, 2001). This signal is deflected by the atmosphere, as a result of refractive index gradients, and received at tracking stations on Earth. After an initial data reduction to eliminate Doppler shifts caused by motion of the spacecraft and Earth, both the deflection of the signal and the resulting Doppler shift in its frequency are analyzed to determine a refractive index profile as a function of the radius of the ray path (with respect to the centre of mass of the planet) and subsequently the number density profile, from which pressure profiles are retrieved by integrating the hydrostatic equation, assuming an appropriate temperature at the upper boundary. Temperature profiles are obtained from the equation of state $T = p/(nk)$, where p is the pressure, n is number density (calculated from the refractive index) and k is the Boltzmann constant. Further details of the procedure are described by Hinson et al. (1999). Since both the topography and geopotential field are well known for Mars, the vertical profiles of temperature and pressure can be related to the local height above the surface and registered accurately within the gravity field.

The vertical profiles of temperature and pressure can be finally related to the local height above the Martian surface, if the local radius of the geoid and the topography are known.

The fractional uncertainty of radio occultation profiles, which extend from

the surface to the 10-Pa pressure level (on average, about 40 km), is about 6% at the top (corresponding to 10 K for temperature and 0.6 Pa for pressure), owing to the uncertainty in the assumed boundary temperature, and 0.4% near the surface (corresponding to 1 K and 2 Pa for temperature and pressure). The uncertainty in radius is unlikely to exceed about 60 m (Hinson et al., 1999), although recent comparisons with Viking Lander pressure measurements suggests that the radius errors are even smaller.

Temperature profiles retrieved by the MGS radio science team have been used in this study for the period of time corresponding to the data assimilation. Fig. 3 is a scatter plot showing the location, in latitude and season, of the radio occultation measurements which have been used. The colour scale refers to the corresponding solar altitude. It is quite evident that the coverage of measurements is not evenly spread, either in latitude and time of the year, whereas a good coverage in longitude was obtained. Most of the measurements are limited to high northern latitudes, but there are measurements at middle-equatorial latitudes in summer, autumn and winter. In the southern hemisphere, however, measurement coverage is poor and mostly limited to spring and winter at middle latitudes. The range of local time is mostly limited to the morning, between 2.00am and 11.00am. Most of the profiles at middle-low latitudes are night profiles, whereas most day time profiles are located at latitudes higher than 60 degrees. Finally, very few measurements are available during the dust storm seasons, but some were taken at middle latitudes during the planet encircling dust storm of 2001 (MY 25).

— Figure 3 —

Assessment of the degree of agreement between the observations and the control simulation and data assimilation was made by comparing temperature profiles as a function of local height. These profiles were extrapolated *a posteriori* from the assimilation and control simulation output files by using linear interpolation in space and time from the nearest model grid points, in order to obtain profiles at the same location, areocentric longitude and local time, as the radio occultation profiles.

4 Comparison of the control simulation and data assimilation to radio occultations

In order to estimate the differences between the model profiles and the radio occultation profiles for any location and time of the year and to discriminate among the different degrees of agreement or disagreement which can occur, we performed a statistical comparison by using the mean difference between model temperatures and observed temperatures averaged over 10 km intervals of height:

$$\overline{\Delta T}_H = \frac{1}{N_H} \sum_{N_H} \left(T_{model} - T_{obs} \right), \tag{3}$$

where H is the height interval (either 0-10 km or 10-20 km or 20-30 km or 30-40 km) and N_H is the number of values in a temperature profile within this range. Since the number of radio occultation observations in any height interval is far larger than the number of model levels within that interval and approximately evenly spaced, we interpolated the model temperature profiles in the vertical to achieve the same resolution as the radio occultation profiles. Note that radio occultation measurements have the largest formal errors (up to 10 K) at the top of the profiles and most profiles have just a few measurements between 30 and 40 km. This range of height is therefore the least significant for comparison.

When comparing model profiles and radio occultation profiles, four main situations can come up: either (1) a very good agreement between the two profiles; or (2) the case in which the model profile represents a good fit to observations on the large-scale, but is not able to capture the detected small-scale lapse rate variations; or (3) a model profile which does not reproduce the right lapse rate; or, finally, (4) the case of a model profile which appears uncorrelated with observations. Cases (1) and (2) can be accepted as consistent representations of the observations (taking into account the resolution of the model), whereas the cases (3) and (4) give evidence for some problem with either the model, the assimilation procedure or the measurements. Note that the latter does not necessarily imply problems with radio occultations; it could equally well reveal problems with TES measurements in the case of the comparison of the results with the assimilation.

We plot in Fig. 4 the probability density functions (PDFs) of the mean temperature difference in the four height ranges, both for the assimilation and the control simulation. All the RO profiles in the dataset (as shown in

Fig. 3) were used to produce these PDFs. This plot gives a general impression of the performance of the assimilation, which is seen to improve on the agreement of the control simulation with the RO observations particularly well below 20 km, in terms of both temperature bias and reduced spread of discrepancies in temperature. In the first two height intervals, in fact, the assimilated anomaly distributions are strongly peaked around zero, compared with a noticeable warm bias in the control simulation, and the tails corresponding to overestimated temperatures in the control simulation are definitely reduced. Between 20 and 40 km altitude the PDFs for the assimilation are still significantly peaked around zero, but the variances are evidently larger and the tails at high temperature differences are not reduced. See the following Table 1 and Table 2 for the statistical values pertinent to the PDFs in Fig. 4.

— Figure 4 —

— Table 1 —

— Table 2 —

Breakdowns of the comparison in latitude and time are provided by Figs. 5 and 6 which show, respectively for the control simulation and the assimilation, the mean temperature difference from corresponding radio occultation measurements as a function of the areocentric longitude. Colours indicate different latitude bands. Most of the temperatures in the bands 50°–70°N and 50°–90°S are overestimated in the control simulation, sometimes by a large amount and at all heights. These are the regions where profiles which are uncorrelated between model and observations were found to occur. On the other hand, the assimilation corrects most of these discrepancies below 20 km (outside the global dust storm), although discrepancies in the values of the lapse rate sometime introduce errors at higher altitude (see section 5 for a detailed analysis of this point). Underestimated temperatures at middle-equatorial and southern latitudes in the control simulation are also mostly corrected by the assimilation. During the global dust storm of MY 25 ($L_S = 185° - 270°$), temperatures are either underestimated or overestimated (depending on the hemisphere) by large amounts in the control simulation (note the large negative spike at $L_S \sim 200°$). This happens because it has no correction to the prescribed dust optical depth to take into account the large

increase of dust loading in the atmosphere which occurs during the storm. The additional assimilation of dust observations, on the other hand, was found to improve the results and limit the underestimation of temperatures in the northern hemisphere at middle latitudes, where the loading of dust in the atmosphere is larger.

— Figures 5 and 6 —

These results are summarized in the PDFs of Figs. 7 and 8 (respectively for the control simulation and the assimilation) where the data have been separated into three subsets: one for the global dust storm in MY 25 ($185° < L_S < 270°$), another one for the low-middle latitudes ($-50° < \text{lat} < 50°$) outside the global storm and the last one for the high latitudes ($\text{lat} > |50°|$). See Fig. 3 for the corresponding values of areocentric longitude. At all heights, assimilation improves the agreement with RO at low-middle latitudes, showing well peaked distributions with standard deviation smoothly increasing from ±3.5 K in the lowest height interval to ±8.0 K between 30 and 40 km (the FWHM goes from 6.7 K to 13.5 K). The standard deviation of the control simulation passes rapidly from ±3.6 K below 10 km to ±6.0 K between 10 and 20 km, up to ±7.0 in the highest range (likewise, the FWHM goes from 7.4 K to 10.9 K in the first two ranges, and up to 14.8 K in the fourth one). The improvement is also significant at high latitudes below 10 km, as the long positive tail is completely eliminated, and reduced by a half between 10 and 20 km. This overestimation of temperatures in the model in the first scale height is linked to an anomalously strong inversion in the first few kilometers over the ground, which seems to be a common feature of high latitude thermal profiles, even during polar nights. This issue is currently under investigation. In the assimilation, the effect of lapse rate differences around 20 km propagates upwards and results in a broader distribution with respect to the control simulation in the highest range, which will be discussed in the next section.

As previously stated, assimilation also improves the cold temperature bias of the control simulation during the planet-encircling dust storm, eliminating overall the negative tails. Nevertheless a warm bias remains, which moves the average of the temperature differences to values around 10 K, depending on the height. This aspect will also be considered in detail in the next section.

— Figures 7 and 8 —

So far in the analysis, we did not consider explicitly the standard deviations of the radio occultation measurements, nor those of the model ("weather variability"). In order to take into account these errors and to give a crude representation of the goodness of fit of the assimilation compared to the control simulation, we perform a statistical χ^2 test which verifies the hypothesis that the model profiles are a good fit to the observed RO profiles. To this aim, we calculate the variable:

$$\chi^2 = \sum_N \frac{(T_{model} - T_{obs})^2}{\sigma^2_{model} + \sigma^2_{obs}}, \tag{4}$$

where N is the number of values in an entire RO profile, T_{obs} is the RO temperature at a certain height, T_{model} is the temperature of either the assimilation or the control simulation, interpolated at the corresponding height of the observation, σ^2_{obs} is the RO variance, and σ^2_{model} is the model variance. The latter is considered as typical "weather variability", and derived from the Mars Climate Database (Lewis et al., 1999) at the corresponding season and location, by using the so-called "MGS dust scenario", or a "dust storm scenario" for the period of the 2001 global dust storm.

If we consider the model profile as a fit to the observed profile, the variable above, with a total variance which is the sum of the independent variances of the model and the observations, follows a χ^2 distribution, and the goodness of fit (which is non-parametric, in this case) can therefore be tested. In particular, a fit is considered statistically good when the reduced chi-squared, namely $\chi^2/(N-1)$ when no parameters are estimated, is close to one. For large N, one expects by chance 50% of the values below this threshold and 50% above.

In Fig. 9 we plot the results of the test for the whole dataset, as a function of areocentric longitudes and latitudes. The upper panels are for the control simulation and the lower ones are for the assimilation. It is evident that the assimilation lowers the values of the reduced chi-squared relative to the control simulation at all L_S and latitudes. This is an indication of the fact that the assimilation produces, in general, better fits than the standalone model, at a parity of total variances. As an example, 35% of the points in the assimilation against 19% in the control simulation lie below the line $\chi^2/(N-1) = 1$. Neither of the two cases show a large percentage, and there are points with very high values of reduced chi-squared both in the control simulation and in the assimilation, but it has to be taken into account that

this test is performed over the entire range of heights of the profiles and that the resolutions of the model and the RO measurements are quite different, and so the model sometimes is not able to reproduce the fine structure of the thermal RO profiles over the entire range of heights. Another factor which has to be considered is the possible underestimation of the model variances in the MCD with the smoothly-varying MGS dust scenario.

— Figure 9 —

It is remarkable, however, that the assimilation is able to produce almost twice as many thermal profiles which can be considered as a good fit to the observations compared to the standalone model, reducing the chi-squared values for most of the others.

5 Analysis of the main biases

As shown in the previous section, the assimilation of TES data improves the agreement between the model and independent RO observations overall, despite the fact that discrepancies with respect to RO observations still remain during the global dust storm and at latitudes around 60°N. In order to understand where these discrepancies originate, we analyse here in detail these two cases.

5.1 Global dust storm

During the 2001 planet-encircling storm, the thermal profiles given by the assimilation are systematically warmer than the radio occultation profiles, on average by 10 K above the lowest scale height. But the origin of this discrepancy is not attributable to any systematic error in the assimilation scheme, as Fig. 10 shows very clearly. Here we plot the PDFs of the temperature differences between profiles in the assimilation and corresponding TES profiles, in the four height intervals, for the latitude range 70°S–70°N during the dust storm event ($L_S = 185° - 210°$). If there was a systematic error in the assimilation, such PDFs would be expected to show the same significant bias, but this is evidently not the case. Such biases as exist with respect to the zero mean are between 2.2 and 3.0 K, with standard deviations between ± 5.2 and ± 7.4 K, depending on the height.

— Figure 10 —

A direct comparison between an ensemble of TES temperature profiles and an ensemble of profiles from the assimilation at approximately the same locations (for the latitude range 20°N–40°N; see caption of Fig. 11 for values of local times) demonstrates that there are no significant differences, either in the mean temperature or in the mean lapse rate, as shown in Fig. 11. On the other hand, this figure exhibits a significant bias in the TES temperatures when compared to the radio occultation temperatures, with RO profiles generally exhibiting a steeper mean lapse rate. This is consistent with the overestimation of temperatures in the assimilation compared with RO above the first scale height. It should be noted that the local times for the TES ensemble are not precisely comparable to those of the radio occultations, although the maximum difference of about 2 hours is likely to be of little importance for night-time profiles between 2 and 4 am local time.

— Figure 11 —

The bias between RO and TES at 30-40 km may simply be due to the choice for the upper boundary temperature, but the effect of changes in the boundary condition diminishes at lower altitude, roughly in inverse proportion to pressure, so the difference at the other altitudes must arise from another source. It is beyond the scope of this paper to explain this discrepancy, but there is certainly need for further work on this subject and results from RO and TES during the dust storm should be interpreted with some caution. All direct comparisons between radio occultation and TES thermal profiles were, in fact, for seasons and locations where the dust opacity was extremely small (Hinson et al., 2004), so the relative performance of the two sounding techniques at larger opacity has never been tested directly. Despite the discrepancies between TES and radio occultations, it is notable that the assimilation based on TES observations is able to reproduce most of the large temperature variability during the 2001 global dust storm event as shown by radio occultation observations, even though each TES profile is much smoother than the radio occultation ones that often exhibit very fine temperature variations and inversions with height, owing to gravity waves and other dynamical structures.

As mentioned in section 2, the TES measured infrared dust opacities have been converted to visible ones before being assimilated. The conversion factor

from 1075 cm^{-1} to mean visible wavelengths has been set to 2.0 (Clancy et al., 1995), although there is some uncertainty in its precise value. The global dust storm represents an interesting event during which high values of optical depth were encountered, and for which tests with different values of this conversion factor can therefore be performed with maximum sensitivity. We used two additional values, 1.5 and 2.5, to represent a plausible range of uncertainty, and compare the results in Fig. 12, where we plot (as in Fig. 10) the PDFs of the mean temperature difference between assimilation and TES profiles in the four intervals of height, together with the PDFs of the mean temperature differences between assimilation and radio occultations in the first scale height. The choice of different values for the visible/infrared ratio of the dust opacities indeed has an impact on the broadening of the PDFs and the shift of the peaks towards overestimated temperatures, except for the case of the first scale height. When this ratio is 1.5, we obtain more peaked distributions. On the other hand, for a value of 2.0, the distributions for the height ranges above the first scale height are slightly overestimated, although the peak relative to the distribution below 10 km is closer to the zero mean. The value of 2.5 produces much broader PDFs with a shift in mean value. These results are in accordance to the fact that dust heating through absorption of visible radiation during a dust storm is larger at higher altitudes, whereas the lower layers of the atmosphere receive less radiation.

When comparing the results of the temperature differences with respect to radio occultations for the three values (lower right panel of Fig. 12), it appears that discrepancies are not strongly dependent on the choice of the visible/infrared ratio. For these reasons, the choice of the value 2.0 for this ratio seems a reasonable compromise, even for the severe case of the global dust storm.

— Figure 12 —

5.2 High latitudes

In the same way as for the case of the global dust storm, if the systematic biases shown by the outputs of the assimilation at latitudes between 50°N and 70°N were due to errors in the assimilation scheme, they would also appear as a bias when plotting the PDFs of the temperature difference between assimilation and TES profiles. Figure 13 demonstrates that this is not the case even at high latitudes: the deviations from a zero mean are between -0.01

and 2.3 K, with standard deviations between ±3.7 and ±5.6 K, depending on the height interval. Also in this case, therefore, the reason for the discrepancies with radio occultation profiles originate in the direct comparison between TES and RO measurements.

— Figure 13 —

We consider the four periods of time when biases above the lowest scale height are larger than average, either due to overestimation or underestimation of temperatures, for latitudes between 50°N and 70°N: $L_S \sim 270° - 300°$ in MY 24, $L_S \sim 300° - 330°$ in MY 25, $L_S \sim 30° - 110°$ and $L_S \sim 200° - 270°$ in MY 26. In Fig. 14 we plot the distribution (as a function of areocentric longitude and in a 10° latitude band around the corresponding radio occultation measurement) of TES temperature measurements which were assimilated, having passed the quality control procedure. It is evident that all the overestimated temperatures in the assimilation around 60°N correspond to regions where the coverage of TES observations during the northern winter season or late autumn is poor, owing to the rejection of retrievals with temperatures below the CO_2 condensation temperature at a given pressure, as detailed in section 2. The assimilation, therefore, follows the standalone model temperatures in the absence of an adequate number of observations, thus explaining the biases for three of the examined ranges out of four.

— Figure 14 —

The agreement with radio occultation measurements might improve when the new, recent release of TES temperature retrievals with fewer (possibly) erroneously supersaturated temperatures is assimilated in future experiments (Smith, M. D., personal communication). Nevertheless, such a bias clearly demonstrates the importance of devising a better representation in the model of the physics of CO_2 condensation and convection in the polar region, especially during the winter season. Both CO_2 clouds and CO_2 supersaturation phenomena can contribute to reducing local temperatures by several degrees (Colaprete et al., 2003; Colaprete et al., 2005), but these effects are not yet implemented in the version of the model which is used here.

The explanation for the underestimation of the temperatures in the northern spring of MY 26 has again to be found in a likely bias of TES temperatures with respect to radio occultations, as shown in Fig. 15. As in Fig. 11, we plot

an ensemble of radio occultation profiles in the range $L_S = 30° - 40°$, between latitudes 50°N and 70°N, together with the corresponding profiles in the control simulation, in the assimilation and an ensemble of TES profiles within nearby locations. Times between the acquisition of RO and TES measurements are not directly comparable, but again the difference is only around 2 hours (see caption). TES profiles in this case typically have steeper vertical temperature gradients than RO profiles, thus suggesting an explanation for the underestimation of temperatures in the assimilation. One possible reason for these discrepancies between RO and TES measurements could be a systematic bias in the upper boundary condition for the RO temperature, which can vary by as much as 10 K.

— Figure 15 —

Hinson et al. (2004) reported a direct comparison of TES and radio occultations at high northern latitudes, but this has mainly been performed in regions and at a time of year when the local times of the two measurements nearly coincided or were very close, thus limiting the comparison to a small sample ($L_S = 46° - 140°$ of MY 25, $L_S = 162° - 192°$ of MY 26 and latitudes between 62°N and 85°N). In that comparison, the agreement between the two measurements was good; our results from the assimilation are consistent with that study, sharing good agreement at those times and locations.

6 Stationary waves

One of the major motivations for performing data assimilation on Mars is to investigate the behaviour of stationary or transient waves and thermal tides, a task which is difficult to achieve with measurements from a single sun-synchronous satellite. The global spatial and temporal coverage of data which we can obtain with assimilation provides enough resolution to extract the properties of such waves.

In this paper we focus upon retrievals of stationary waves. The validation of results on the waves in the assimilation can be indirectly deduced from the validation of the thermal profiles, but it would be obviously preferable to have a direct way to verify the former. Hinson et al. (2003, 2004) performed an analysis of stationary waves in radio occultation measurements at four different locations and times of year, one in the southern hemisphere and three in the north. This analysis can be directly compared with the same

analysis in the data assimilation, and results from the latter can therefore be verified.

The four comparisons have been carried out respectively for $L_s = 150°$–$160°$ at latitude 67°S in MY 24 and for $L_s = 52°$–$58°$ at latitude 62°N, $L_s = 76°$–$82°$ at latitude 65°N and $L_s = 99°$–$109°$ at latitude 75°N in MY 25.

Each comparison is performed by using the stationary component of the temperature field, i.e., the average of temperature over the indicated period of L_S, from which the zonal average has been subtracted. It is also possible to compare directly the wave-1 and wave-2 components of the temperature field, obtained through a fourth-order decomposition at each pressure level, in a way consistent with the analysis included in Hinson et al. (2003). The temperature deviation field is represented as the sum of four zonal harmonics:

$$T'(\lambda, p) = \sum_{s=1}^{4} C_s(p) \cos[s\lambda - \gamma_s(p)]], \tag{5}$$

where p is the pressure level, λ is the longitude, and C_s and γ_s are the amplitude and phase, respectively, at zonal wavenumber s. Amplitudes and phases of the four harmonics can be calculated through least squares analysis.

When comparing stationary waves between assimilation and radio occultations in the northern hemisphere, the agreement appears to be excellent. Fig. 16 shows the temperature deviation field and the wave-1 component (which is the dominant component here) for the cases listed above, which can be directly compared to Figs. 10–12 in Hinson et al. (2004). The atmosphere at this northern latitude and time of the year (late spring-early summer) is more zonally uniform than the corresponding case in the southern hemisphere, with a large impact of the wave-1 component on the thermal structure. This is especially so in the case of early summer ($L_s = 99°$–$109°$), which shows well established extrema at about 100 Pa (20 km altitude). In all three cases, the temperature deviation fields in the assimilation describe stationary waves which have the same characteristics and zonal distribution as RO waves. Nonetheless, the model does not resolve sharp vertical variations of temperature, nor do the TES measurements. Therefore, such variations which are present in RO measurements are not included in the data assimilation results, as expected. Waves in the assimilation thus appear smoother than those in RO observations.

— Figure 16 —

Fig. 17 shows the temperature field, the temperature deviation field and the two wave components (s=1 and s=2) for the case of the southern hemisphere in late winter, and can be directly compared to Figs. 5–6 in Hinson et al. (2003). This case is particularly interesting, although pathological, because it shows how the model can be extremely sensitive to the environmental conditions in the polar regions, and how the assimilation of data below a certain altitude impacts at higher altitudes.

— Figure 17 —

The most striking feature which can be observed in the temperature field of Fig. 17 is the strong polar warming which occurs at 20–30 Pa (about 25–30 km), much lower in altitude than the corresponding one in the RO temperature field. This in turn is reflected in the form of the wave-1 and wave-2 components of the temperature deviation field, which show, respectively, local extrema and inversions at about 20 Pa. Such features are not present at that pressure level in the radio occultation measurements, where they seem to be positioned at a much higher altitude, as would be expected. Nonetheless, apart from this compression of the temperatures towards lower altitudes, the general form and values of the waves compare well to those of radio occultations, showing good zonal agreement on the positions of local maxima and minima. Also the intrusion of warm temperatures around 60°E at much lower altitudes is well represented in the assimilation and reflects itself in the maximum of the temperature deviations and wave-1 component, although much lower in altitude than in the RO.

A further analysis of the temperature profiles involved in this comparison is shown in Fig. 18, and explains why the temperature field is anomalously warm at 30 km. When comparing the control simulation to RO, it is evident that the temperature in the first levels of the model near the surface is, on average, $\sim$ 15 K warmer, with quite a strong inversion in the first few kilometers altitude. This inversion is stronger around 180°E and occurs on an area of the planet which is still covered by CO_2 ice, although is no more in the polar night. Note that the surface temperature of the control simulation profiles in the figure is that of CO_2 ice (about 150 K), but because of the strong inversion in the lowest few levels of the model, this cannot be appreciated in the figure. Such an inversion does not seem to have a counterpart in the radio occultation measurements, and is a feature of the GCM which is under investigation at the moment, as it appears to be a major characteristic

of the temperature profiles at high latitudes, even during the polar nights. Data assimilation corrects this huge overestimation of temperatures in the lower atmosphere, but since the balance among all the variables in the model must be globally maintained and there is no assimilation of data above 40 km altitude, it is necessary to compensate for the cooling near the surface by introducing an anomalous polar warming at low altitudes, from 25 km (about 30 Pa) upwards. An improvement might arise from the assimilation of TES limb thermal profiles, which have become available recently, and extend to higher altitudes, up to approximately 60 km. This is also an example of how data assimilation can be used to discover possible errors or problems in the model.

— Figure 18 —

7 Conclusions

This paper describes the validation against radio occultation measurements of the results of a data assimilation performed for the Martian atmosphere by using MGS/TES retrievals of thermal profiles and total dust opacities below 40 km altitude. It provides also an intercomparison of the different datasets involved in this study (MGS/TES, MGS/radio occultation, data assimilation and control simulation) and an analysis of the main biases which affect them.

Results from comparison with radio occultation measurements are far from being conclusive, given the uneven global coverage in space and time of this type of observations. Nevertheless, they provide evidence of the fact that, overall, data assimilation improves the agreement of the results of the free-running GCM with RO measurements, in particular below 20 km altitude, where the latter appear to be more accurate. A chi-squared test performed over the entire dataset to verify the hypothesis that the model profiles are a good fit to the RO profiles showed that data assimilation is able to lower the values of the chi-squared compared to the standalone model at all latitudes and areocentric longitudes, providing almost twice as many profiles which can be considered good fits to the RO profiles than the control simulation.

There are regions where the performance of the assimilation does not appear to be enhanced with respect to the independent standalone GCM, and these cases were analysed in detail. In particular, the thermal profiles from the assimilation show important discrepancies with respect to the corresponding radio occultation profiles during the planet-encircling dust storm of

MY 25 (June-October 2001) and at high northern latitudes, around 60°N, in winter-early spring. These discrepancies underline possible problems either in the GCM or in the measurements (TES retrievals and/or radio occultation measurements), and extend the importance of the work presented here to the validation of the consistency of the two sets of observations, once it has been demonstrated that the assimilation technique itself is not intrinsically biased.

The discrepancies arising at high latitudes and mostly during the winter season may derive from an inadequate representation in the GCM of microphysical processes such as CO_2 clouds, convection and/or supersaturation (Colaprete et al., 2003). Future work will aim to solve these problems and improve the physical scheme in the polar regions of the model. These discrepancies could, on the other hand, derive from problems in the retrievals of TES thermal profiles, as recent communications from the TES retrieval group at Goddard Space Flight Centre have suggested. In this case, the assimilation might improve further with the use of the new, recent release of recalibrated TES data (end of 2005). Future assimilation experiments will include these corrected thermal profiles, and a forthcoming paper will address the subject of the validation of the new TES release and data assimilation.

The discrepancies during the 2001 global dust storm appear to reflect a fundamental inconsistency between the TES and RO retrievals under dusty conditions, particularly at altitudes below about 30 km, which should be investigated further.

We also performed a validation against radio occultation measurements of the properties of stationary waves at four different locations and time of year. The study of wave behaviour is one of the major objectives for which data assimilation is performed on Mars, where results from a single sun-synchronous satellite alone are not sufficient for determining the properties of transient waves or thermal tides. This paper shows that stationary waves in the assimilation at the studied locations exhibit good agreement with RO measurements, and that discrepancies are mainly due to problems in the standalone GCM which are currently under investigation, rather than biases in the assimilation technique. These results, therefore, support the use of assimilation as powerful and reliable technique for the scientific investigation of waves on Mars.

It is worth noting that limb retrievals from TES have become available recently. They might improve the results of the assimilation, since the vertical extension of the thermal profiles is higher in altitude than the nadir soundings (reaching around 60 km), although the number of limb profiles is quite limited

in space and time.

Future work will also take advantage of data on the vertical structure of the dust distribution, or at least its vertical extent, which at the moment are prescribed as they are inferred from indirect considerations of particle sedimentation and eddy mixing. The Mars Climate Sounder experiment aboard the NASA "2005 Mars Reconnaissance Orbiter" should provide such an improvement in the coverage of vertical dust distributions (Taylor et al., 2006) in due course.

Acknowledgements

The authors gratefully acknowledge the use of TES temperature and dust opacity retrievals provided by B. J. Conrath, J. C. Pearl and M. D. Smith of Goddard Space Flight Center, Greenbelt, Maryland (USA). They thank, in particular, M. D. Smith for his insightful comments on the manuscript.

LM is grateful for support from the UK Particle Physics and Astronomy Research Council.

References

Banfield, D., Ingersoll, A., Keppenne, C., 1995. A steady-state Kalman filter for assimilating data from a single polar-orbiting satellite. J. Atmos. Sci. 52, 737–753.

Clancy, R. T., Lee, S. W., Gladstone, G. R., McMillan, W. W., Rousch, T., 1995. A new model for Mars atmospheric dust based upon analysis of ultraviolet through infrared observations from Mariner 9, Viking, and Phobos. J. Geophys. Res. 100, 5251–5263.

Clancy, R. T., Sandor, B. J., Wolff, M. J., Christensen, P. R., Smith, M. D., Pearl, J. C., Conrath, B. J., Wilson, R. J., 2000. An intercomparison of ground-based millimiter, MGS TES, and Viking atmospheric temperature measurements: Seasonal and interannual variability of temperatures and dust loading in the global Mars atmosphere. J. Geophys. Res. 105, 9553–9571.

Clancy, R. T., Wolff, M. J., Christensen, P. R., 2003. Mars aerosol studies with the MGS TES emission phase function observations: Optical depths,

particle sizes, and ice cloud types versus latitude and solar longitude. J. Geophys. Res. 108 (E9), 2–1.

Colaprete, A., Haberle, M. R., Toon, B. O., 2003. Formation of convective carbon dioxide clouds near the south pole of Mars. J. Geophys. Res. 108, 17–1.

Colaprete, A., Haberle, R. M., Barnes, J. R., Dec. 2005. CO2 Clouds, CAPE and convection on Mars: Observations and General Circulation Modeling. AGU Fall Meeting Abstracts, C5+.

Conrath, B. J., Pearl, J. C., Smith, M. D., Maguire, W. C., Dason, S., Kaelberer, M. S., Christensen, P. R., 2000. Mars Global Surveyor Thermal Emission Spectrometer (TES) observations: Atmospheric temperatures during aerobraking and science phasing. J. Geophys. Res. 105, 9509–9519.

Forget, F., Hourdin, F., Fournier, R., Hourdin, C., Talagrand, O., Collins, M., Lewis, S. R., Read, P. L., Hout, J.-P., 1999. Improved general circulation models of the martian atmosphere from the surface to above 80 km. J. Geophys. Res. 104, 24,155–24,176.

Forget, F., Wanherdrick, Y., Lewis, S. R., 2001. Validation of the Mars General Circulation Model and Climate Database with new spacecraft observations. Technical Note, contract 11369/95/NL/JG. Work Package 7, ESA.

Hinson, D. P., 2006. Radio occultation measurements of transient eddies in the northern hemisphere of mars. J. Geophys. Res.In press.

Hinson, D. P., Simpson, R. A., Twicken, J. D., Tyler, G. L., 1999. Initial results from radio occultation measurements with Mars Global Surveyor. J. Geophys. Res. 104 (E11), 26,997–27,012.

Hinson, D. P., Smith, M. D., Conrath, B. J., 2004. Comparison of atmospheric temperature obtained through infrared sounding and radio occultation by Mars Global Surveyor. J. Geophys. Res. 109 (E18), 12002–+.

Hinson, D. P., Tyler, G. L., Hollingsworth, J. L., Wilson, R. J., 2001. Radio occultation measurements of forced atmospheric waves on Mars. J. Geophys. Res. 106 (E1), 1463–1480.

Hinson, D. P., Wilson, R. J., Smith, M. D., Conrath, B. J., 2003. Stationary planetary waves in the atmosphere of Mars during southern winter. J. Geophys. Res. 108, 4–1.

Houben, H., 1999. Assimilation of Mars Global Surveyor meteorological data. Adv. Space Res. 23 (11), 1899–1902.

Kass, D. M., Ingersoll, A. P., 1997. Assimilation of MGS data into the Ames Mars GCM. EOS 78.

Lewis, S. R., Barker, P. R., 2005. Atmospheric tides in a Mars general circulation model with data assimilation. Adv. Space Res. 36 (11), 2162–2168.

Lewis, S. R., Collins, M., Read, P. L., 1996. Martian atmospheric data assimilation with a simplified general circulation model: Orbiter and lander networks. Planet. Space Sci. 44, 1395–1409.

Lewis, S. R., Collins, M., Read, P. L., 1997. Data assimilation with a martian atmospheric gcm: An example using thermal data. Adv. Space Res. 19 (8), 1267–1270.

Lewis, S. R., Collins, M., Read, P. L., Forget, F., Hourdin, F., Fournier, R., Hourdin, C., Talagrand, O., Huot, J.-P., 1999. A climate database for Mars. J. Geophys. Res. 104 (E10), 24,177–24,194.

Lewis, S. R., Read, P. L., 1995. An operational data assimilation scheme for the Martian atmosphere. Adv. Space Res. 16 (6), 9–13.

Lewis, S. R., Read, P. L., Conrath, B. J., Pearl, J. C., Smith, M. D., 2005. Assimilation of Thermal Emission Spectrometer atmospheric data during the Mars Global Surveyor aerobraking period. IcarusSubmitted.

Lorenc, A. C., Bell, R. S., Macpherson, B., 1991. The Meteorological Office analysis correction data assimilation scheme. Quart. J. R. Meteor. Soc. 117, 59–89.

Martin, T. Z., 1986. Thermal infrared opacity of the Mars atmosphere. Icarus 66, 2–21.

Montabone, L., Lewis, S. R., Read, P. L., 2005. Interannual variability of Martian dust storms in assimilation of several years of Mars Global Surveyor observations. Adv. Space Res. 36 (11), 2146–2155.

Smith, M. D., 2004. Interannual variability in TES atmospheric observations of Mars during 1999-2003. Icarus 167, 148–165.

Smith, M. D., Pearl, J. C., Conrath, B. J., Christensen, P. R., 2000. Mars Global Surveyor Thermal Emission Spectrometer (TES) observations of dust opacity during aerobraking and science phasing. J. Geophys. Res. 105, 9539–9552.

Smith, M. D., Pearl, J. C., Conrath, B. J., Christensen, P. R., 2001. One martian year of atmospheric observations by the thermal emission spectrometer. Geophys. Res. Lett. 28 (22), 4263–4266.

Taylor, F. M., Calcutt, S. B., Read, P. L., Lewis, S. R., McCleese, D. J., Schofield, J. T., Zurek, R. W., 2006. Atmospheric temperature sounding on Mars, and the climate sounder on the 2005 Reconnaissance orbiter. Adv. Space Res.In press.

Zhang, K. Q., Ingersoll, A. P., Kass, D. M., Pearl, J. C., Smith, M. D., Conrath, B. J., Haberle, R. M., 2001. Assimilation of Mars Global Surveyor atmospheric temperature data into a general circulation model. J. Geophys. Res. 106, 32,863–32,877.

Tables

	0-10 km	10-20 km	20-30 km	30-40 km
Average	4.69	4.64	4.33	2.61
Std	7.26	7.84	8.63	8.71
Skewness	0.96	0.52	0.62	1.05
Kurtosis	0.79	0.45	1.92	2.99
FWHM	6.52	15.78	12.74	12.48

Table 1: Statistical values for the PDFs of the mean temperature difference between control simulation and radio occultation, see Fig. 4

	0-10 km	10-20 km	20-30 km	30-40 km
Average	1.12	1.12	1.89	0.59
Std	4.14	6.30	8.76	9.92
Skewness	0.72	0.66	0.71	0.62
Kurtosis	6.14	0.72	0.77	0.95
FWHM	5.59	7.86	11.72	12.70

Table 2: Statistical values for the PDFs of the mean temperature difference between assimilation and radio occultation, see Fig. 4

Figure captions

Figure 1. In the independent GCM control simulation, the dust scenario is prescribed by the dust optical depth in the visible at 700 Pa (upper panel) and the altitude of the top of the dust (lower panel), defined to be the height at which the dust mixing ratio falls to 1/1000 of its well-mixed value in the lower atmosphere. These two parameters are plotted as functions of areocentric longitude and latitude. In panel (b), contour labels are in km.

Figure 2. TES observations which have been used in the assimilation. The upper panel (a) shows the period of time spanned by MGS orbits in the mapping phase, for which there are available TES observations which have been assimilated: from Orbit Counter Keeper (OCK) number 2543 (May 1999) until OCK number 25966 (August 2004). Martian years (MY) are identified by a number near the corresponding branch. The lower panel (b) shows the number of thermal profiles and dust optical depth observations per mapping day which passed the quality control procedure and were assimilated. Note that the OCK numeration follows the TES team convention, and not the Mars Surveyor Project (MSP) convention which reset the orbit count to zero after orbit 1683 (the official start of mapping operations).

Figure 3. Distribution of available radio occultation thermal profiles in latitude, areocentric longitude and solar altitude (height of the Sun over the horizon). Colours refer to different solar altitudes in degrees (blueish colours are for night profiles, yellowish colours for daylight profiles). Martian years are identified in the same way as in Fig. 2.

Figure 4. Probability density functions of the mean temperature difference between either the control simulation and the radio occultation profiles (dashed lines) or the assimilation and the radio occultation profiles (solid

lines). PDFs are given for four ranges of height, for the entire RO dataset.

Figure 5. Distribution of mean temperature difference between the control simulation and the radio occultation profiles as a function of areocentric longitude. Colours refer to different latitude bands. Note that the negative spike after $L_S = 180°$ in MY 25 is the footprint of the 2001 global dust storm ($L_S \sim [185° - 270°]$).

Figure 6. Same as in Fig. 5, but for the mean temperature difference between assimilation and radio occultation profiles.

Figure 7. Probability density functions of the mean temperature difference between control simulation and radio occultation profiles for three subsamples: observations made during the global dust storm ($L_S = [185°, 270°]$ in MY 25), observations in the low-middle latitudes (between 50°S and 50°N) and observations at high latitudes ($> |50°|$).

Figure 8. Same as in Fig. 7, but for the mean temperature difference between assimilation and radio occultation profiles.

Figure 9. Values of reduced chi-squared for the entire dataset of radio occultation thermal profiles. The upper panels are for the control simulation (as a function of areocentric longitude to the left and latitudes to the right) and the lower ones are for the assimilation. The horizontal line indicates the value of $\chi^2/(N-1) = 1$. A good fit of a model profile to the corresponding RO profile is determined by a value of reduced chi-squared close to one.

Figure 10. Probability density functions of the mean temperature difference between assimilation and TES in the four height intervals. The comparison is performed in the latitude range 70°S–70°N during the global dust storm event of MY 25 ($L_S = 185° - 210°$). The temperature profiles of the model are calculated at the same position and local time as the TES observations.

Figure 11. Plot of an ensemble of profiles for radio occultation, TES, control simulation and assimilation in the latitude range 20°N–40°N during the global dust storm event of MY 25. TES profiles are collected in a 1° interval of areocentric longitude, 0.5° interval of latitude, and 4° interval of longitude with respect to RO profiles. Local times are in the range 4:32–4:56 a.m for RO and 2:46–2:51 a.m. for TES. The thick superimposed lines are the averaged profiles.

Figure 12. Three panels of this figure (the two upper ones and the lower left one) show the PDFs of the mean temperature difference between assimilation and TES in the four height intervals, for three different values of the ratio visible/infrared of the dust optical depth: 1.5, 2.0 and 2.5. The comparison

is performed in the latitude range 70°S–70°N during the global dust storm event, as in Fig. 10. The lower right panel shows the PDFs of the mean temperature difference between assimilation and radio occultations in the first scale height (below 10 km), for the same three values. The range of areocentric longitudes is that of the global dust storm: $L_S = [185°, 270°]$ in MY 25.

Figure 13. Same as in Fig. 10, but for the latitude range 50°N–70°N at all areocentric longitudes.

Figure 14. Distributions of TES temperature observations, which were assimilated having passed the quality control procedure, in areocentric longitudes and in a 10° latitude band around the corresponding radio occultation measurement. The distributions are shown for four periods of time, as indicated in the figure.

Figure 15. Same as in Fig. 11, but for the latitude range 50°N–70°N and the areocentric range $L_S = 30° - 40°$ in MY 26. TES profiles are collected in a 1° interval of areocentric longitude, 0.2° interval of latitude, and 4° interval of longitude with respect to RO profiles. Local times are in the range 4:08–4:24 a.m. for RO and 2:07–2:11 a.m. for TES. The thick lines are the averaged profiles.

Figure 16. Temperature deviation fields and wave-1 components in the assimilation at three different northern latitudes and time of year. The upper panels are for the case at 62°N and $L_S = [52°, 58°]$, the central panels are for the case at 65°N and $L_S = [76°, 82°]$, and the lower panels are for the case at 75°N and $L_S = [100°, 108°]$, all in MY 25. They can be directly compared to, respectively, Figs. 10, 11 and 12 in Hinson et al. (2004) for the case of radio occultations. The pressure range is 610–10 Pa. Contour levels are separated by 1 K. Shaded areas and dashed contours are for negative values.

Figure 17. Temperature field, temperature deviation field, wave-1 and wave-2 components at 67°S in the assimilation, for the range $L_S = [150°, 160°]$ in MY 24. Pressures are shown in the range 400–10 Pa. Surface pressure has an average value of 430 Pa and a minimum value of 357 Pa. Contour levels in the temperature deviation field and in the two wave components are separated by 1 K. Shaded areas and dashed contours indicate negative values. This figure can be directly compared to Figs. 5–6 in Hinson et al. (2003) for the corresponding case in radio occultation observations.

Figure 18. Ensemble of profiles for radio occultation, TES, control simulation and assimilation in the L_S range 150°–160° in MY 24, around latitude 67°S. TES profiles are collected in a 1° interval of areocentric longitude, 10°

interval of latitude, and 4° interval of longitude with respect to RO profiles. Local times are in the range 9:41–10:37 a.m for RO, whereas for TES they are distributed in two narrow intervals around, respectively, 2 a.m. and 3 p.m. TES and RO are therefore not directly comparable in this case, but they are plotted for reference. The thick superimposed lines are the averaged profiles.

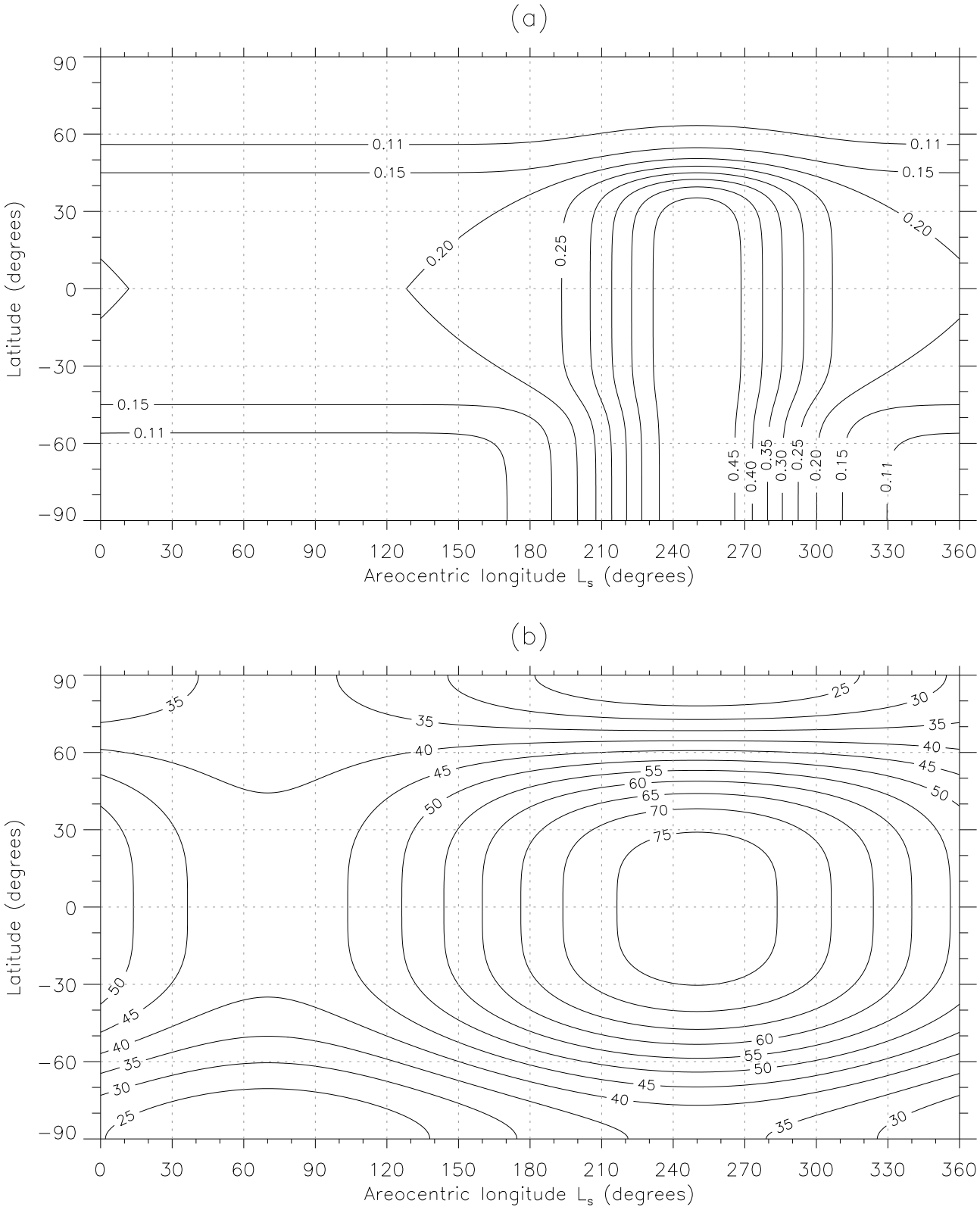

Figure 1: Montabone et al., Validation of MGS/TES data assimilation

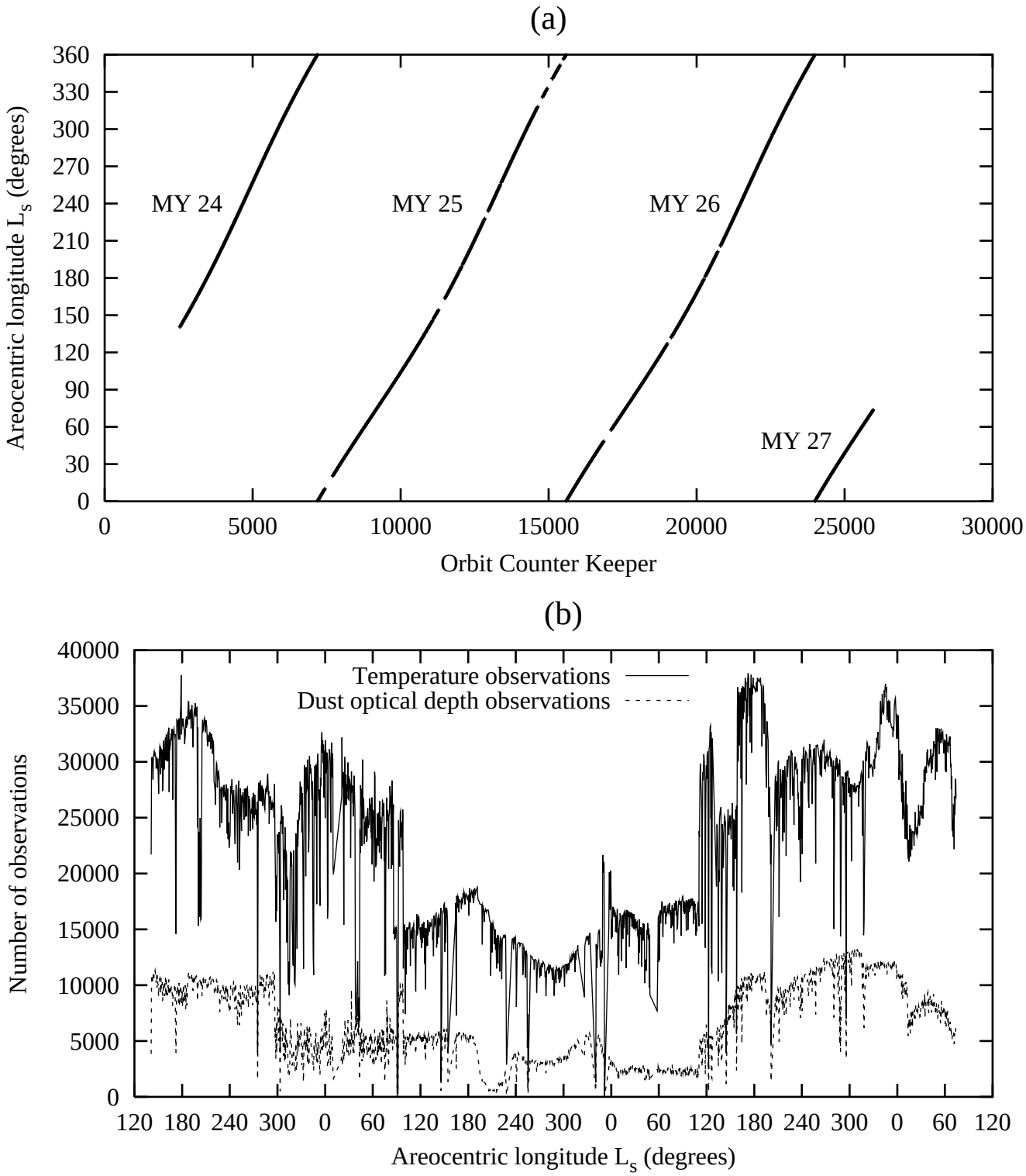

Figure 2: Montabone et al., Validation of MGS/TES data assimilation

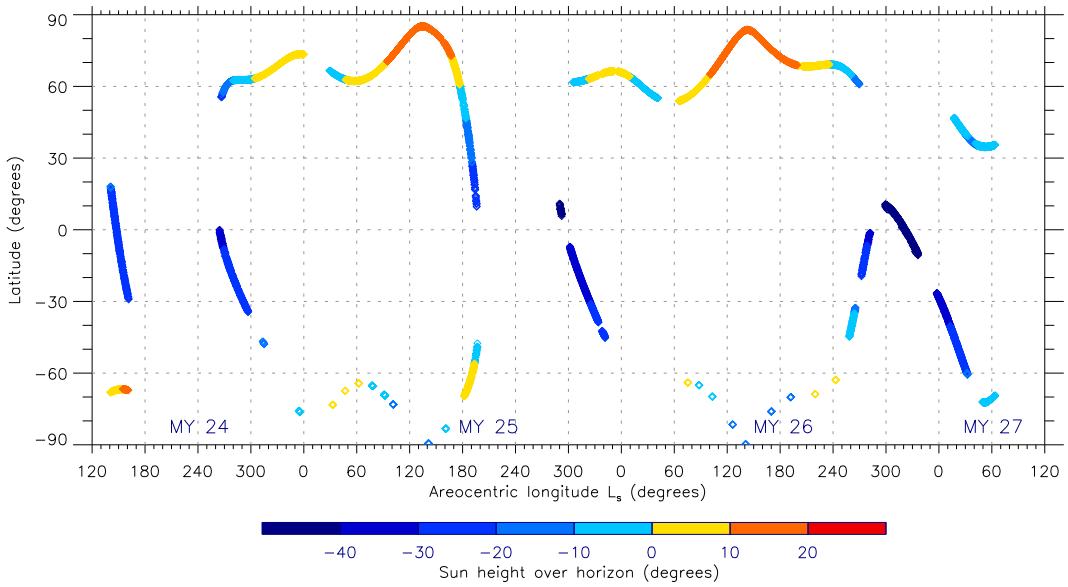

Figure 3: Montabone et al., Validation of MGS/TES data assimilation

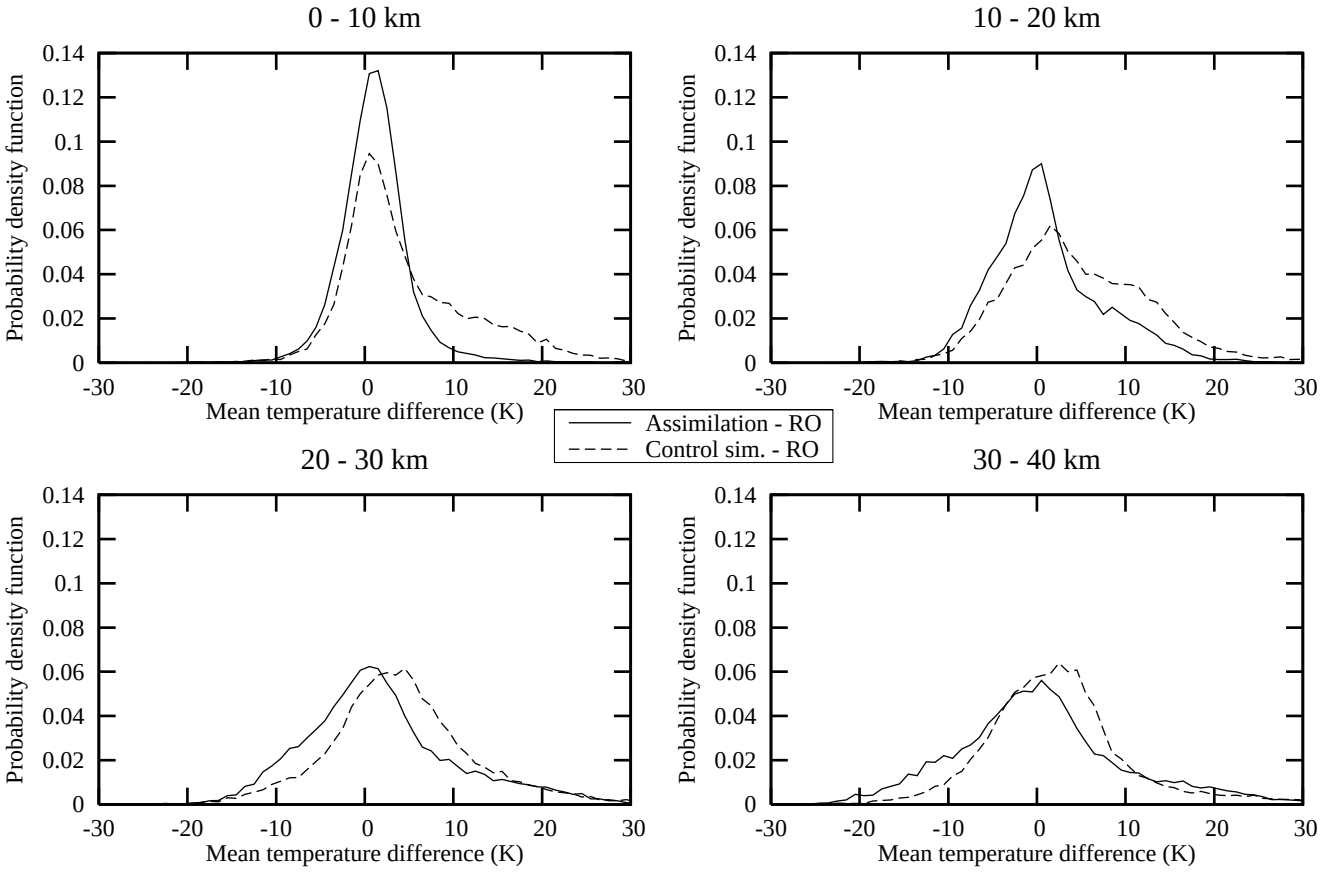

Figure 4: Montabone et al., Validation of MGS/TES data assimilation

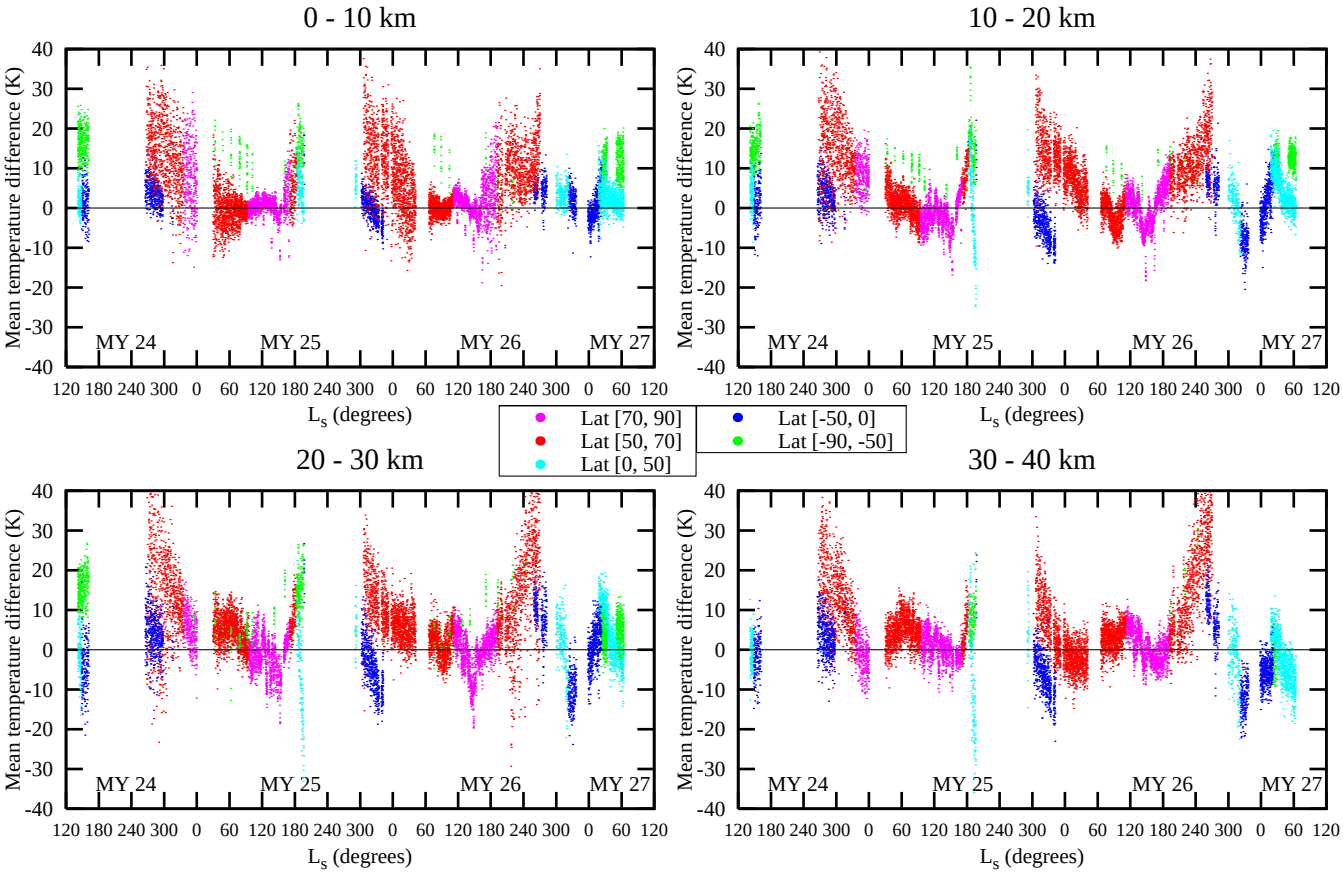

Figure 5: Montabone et al., Validation of MGS/TES data assimilation

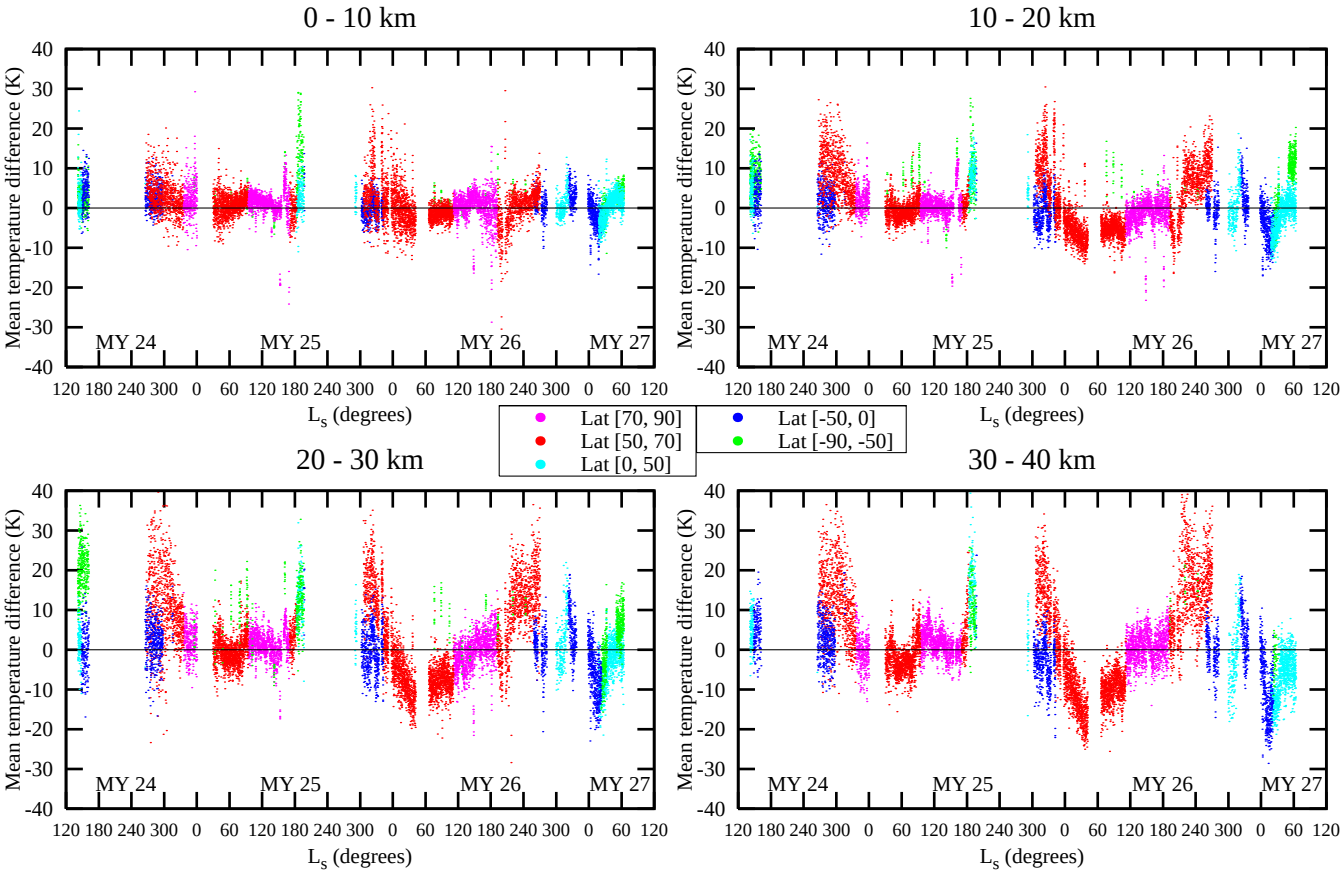

Figure 6: Montabone et al., Validation of MGS/TES data assimilation

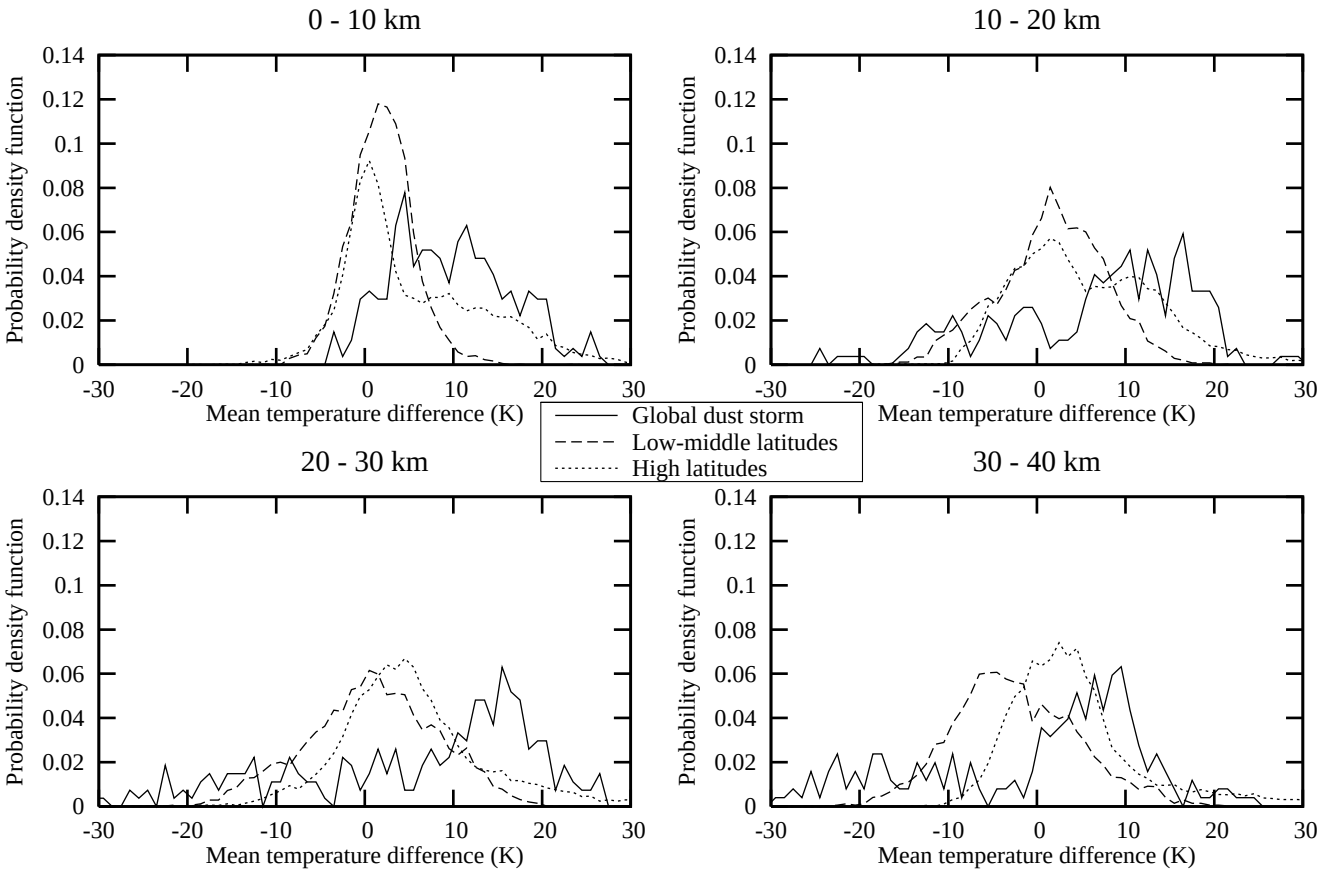

Figure 7: Montabone et al., Validation of MGS/TES data assimilation

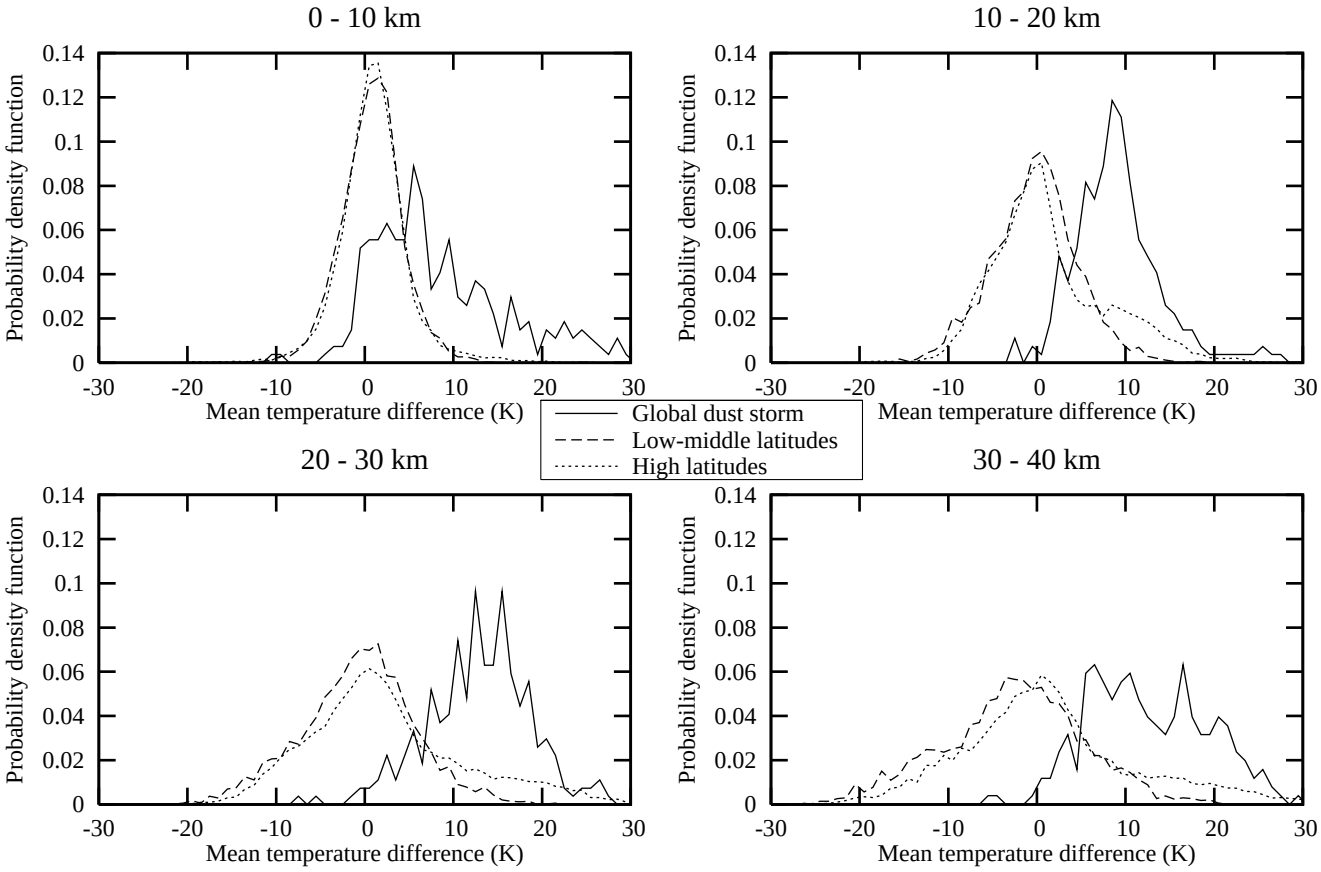

Figure 8: Montabone et al., Validation of MGS/TES data assimilation

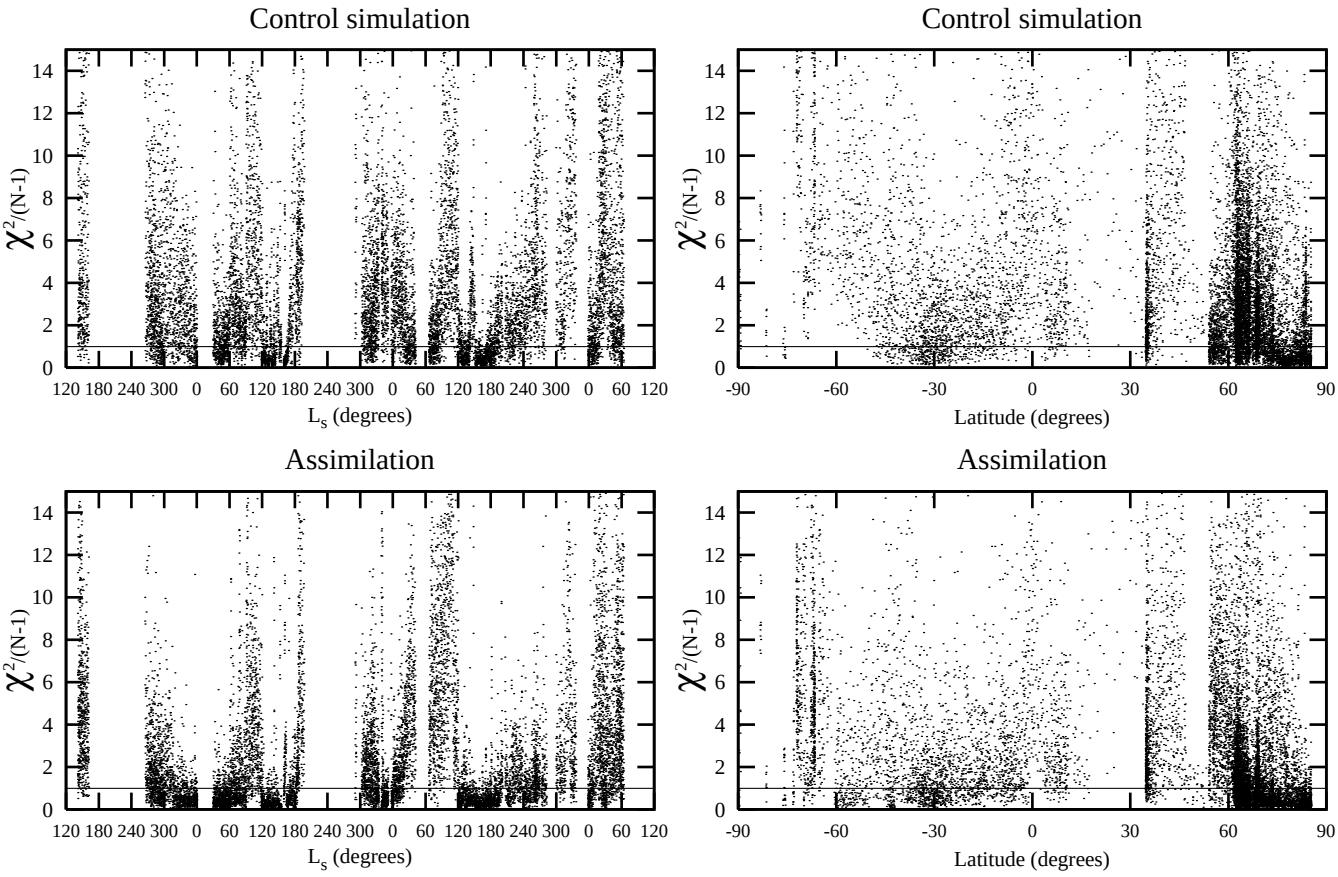

Figure 9: Montabone et al., Validation of MGS/TES data assimilation

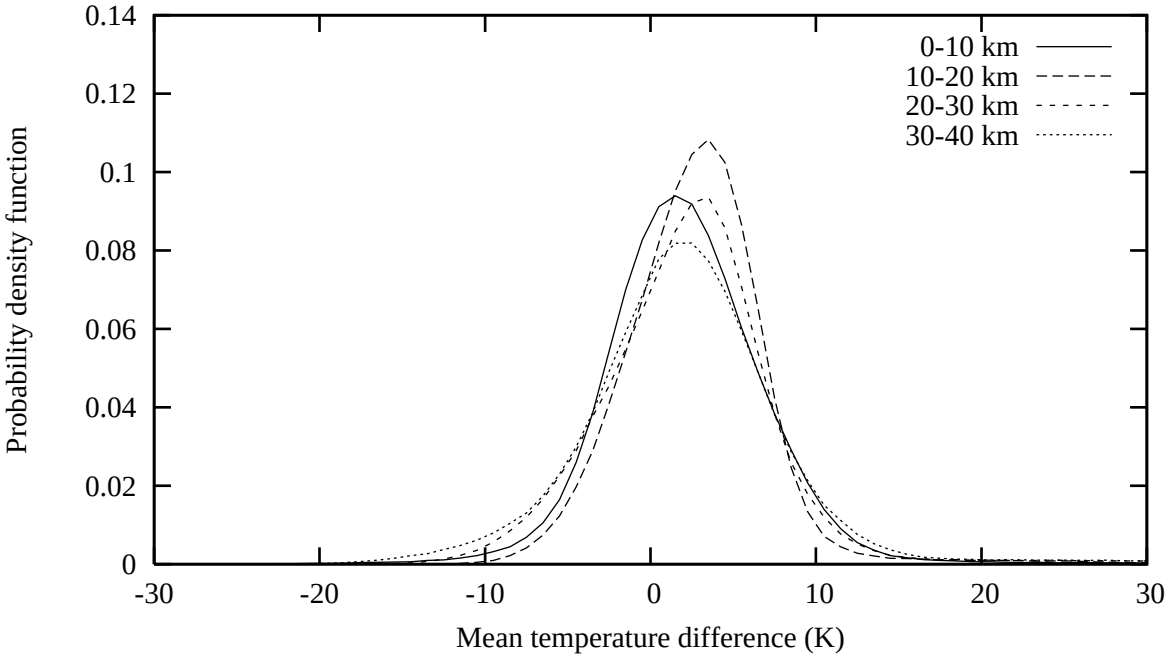

Figure 10: Montabone et al., Validation of MGS/TES data assimilation

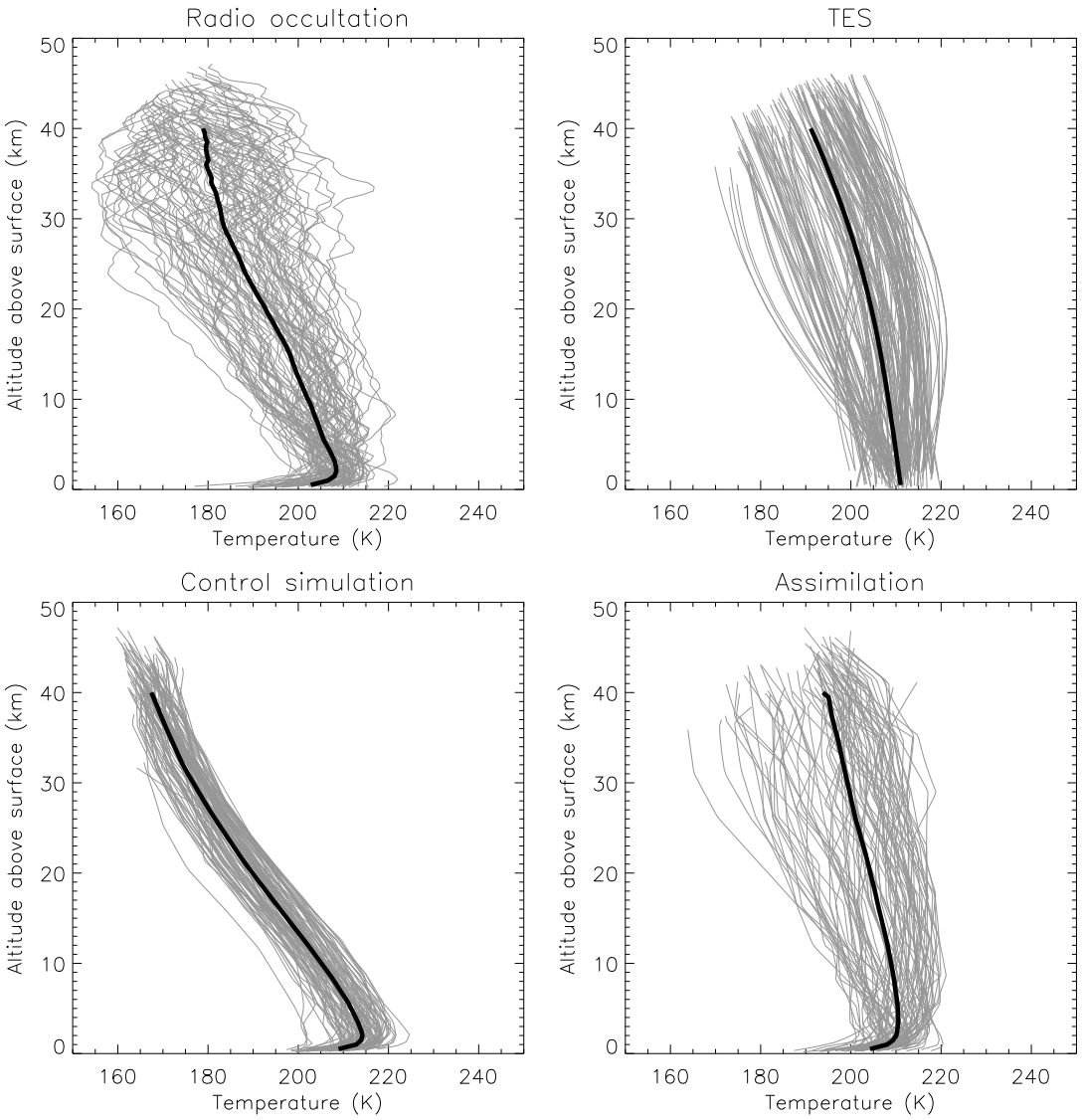

Figure 11: Montabone et al., Validation of MGS/TES data assimilation

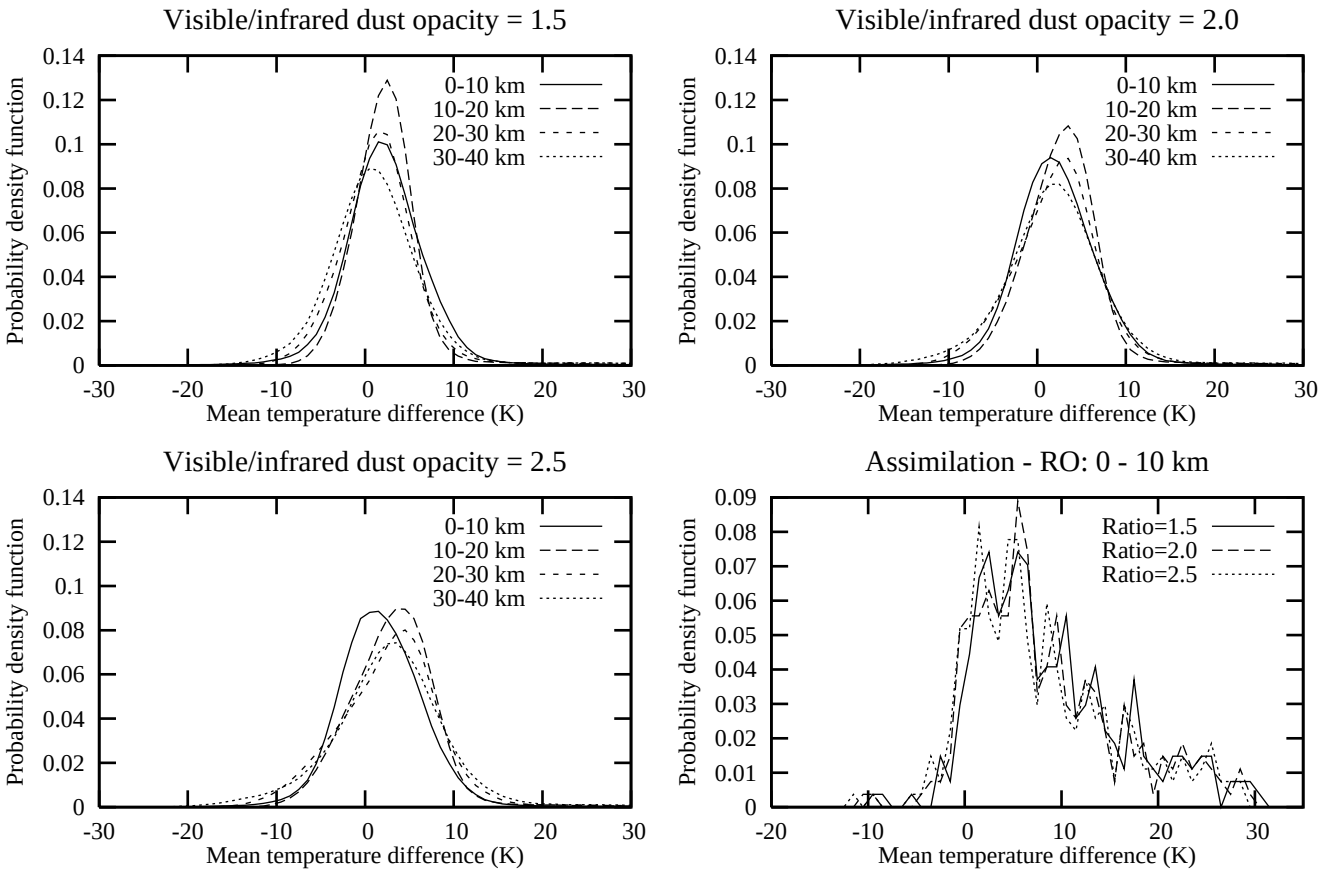

Figure 12: Montabone et al., Validation of MGS/TES data assimilation

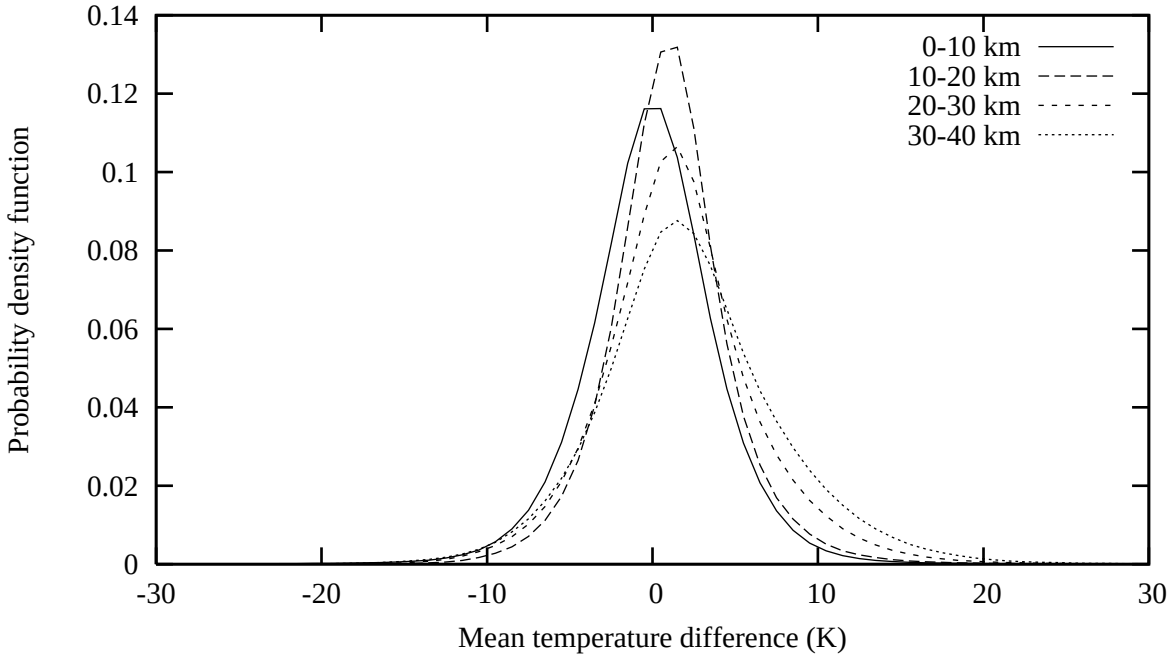

Figure 13: Montabone et al., Validation of MGS/TES data assimilation

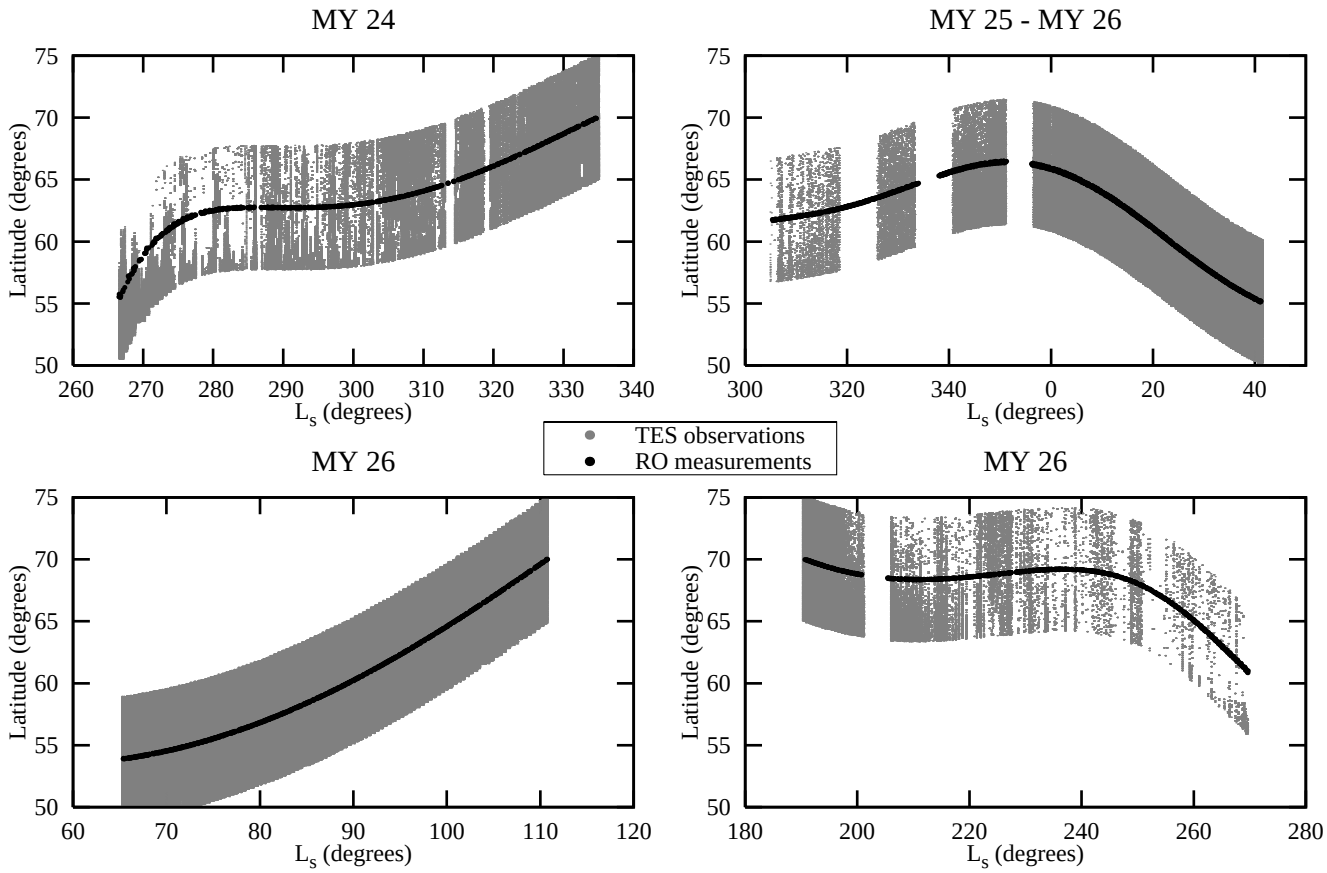

Figure 14: Montabone et al., Validation of MGS/TES data assimilation

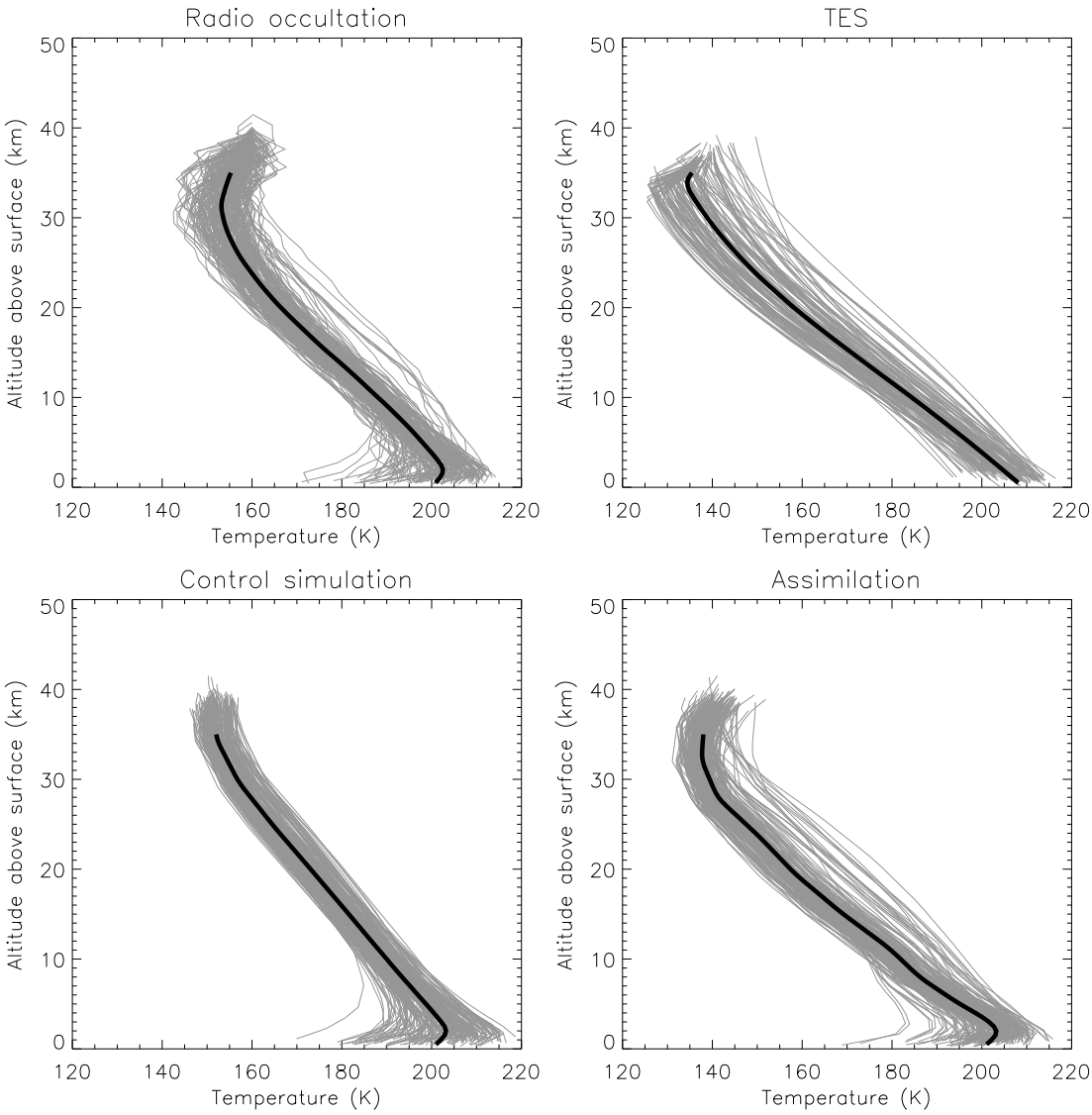

Figure 15: Montabone et al., Validation of MGS/TES data assimilation

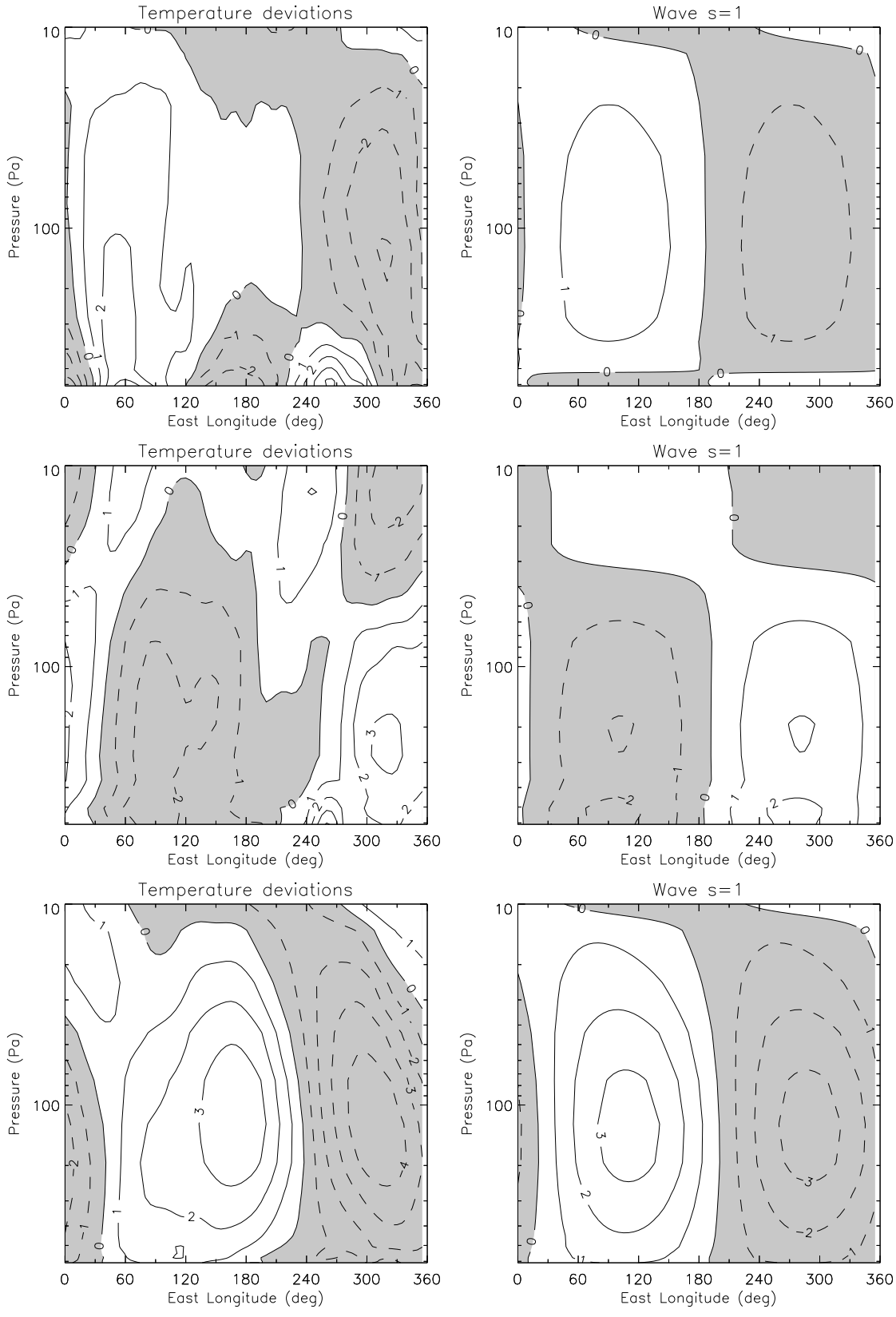

Figure 16: Montabone et al., Validation of MGS/TES data assimilation

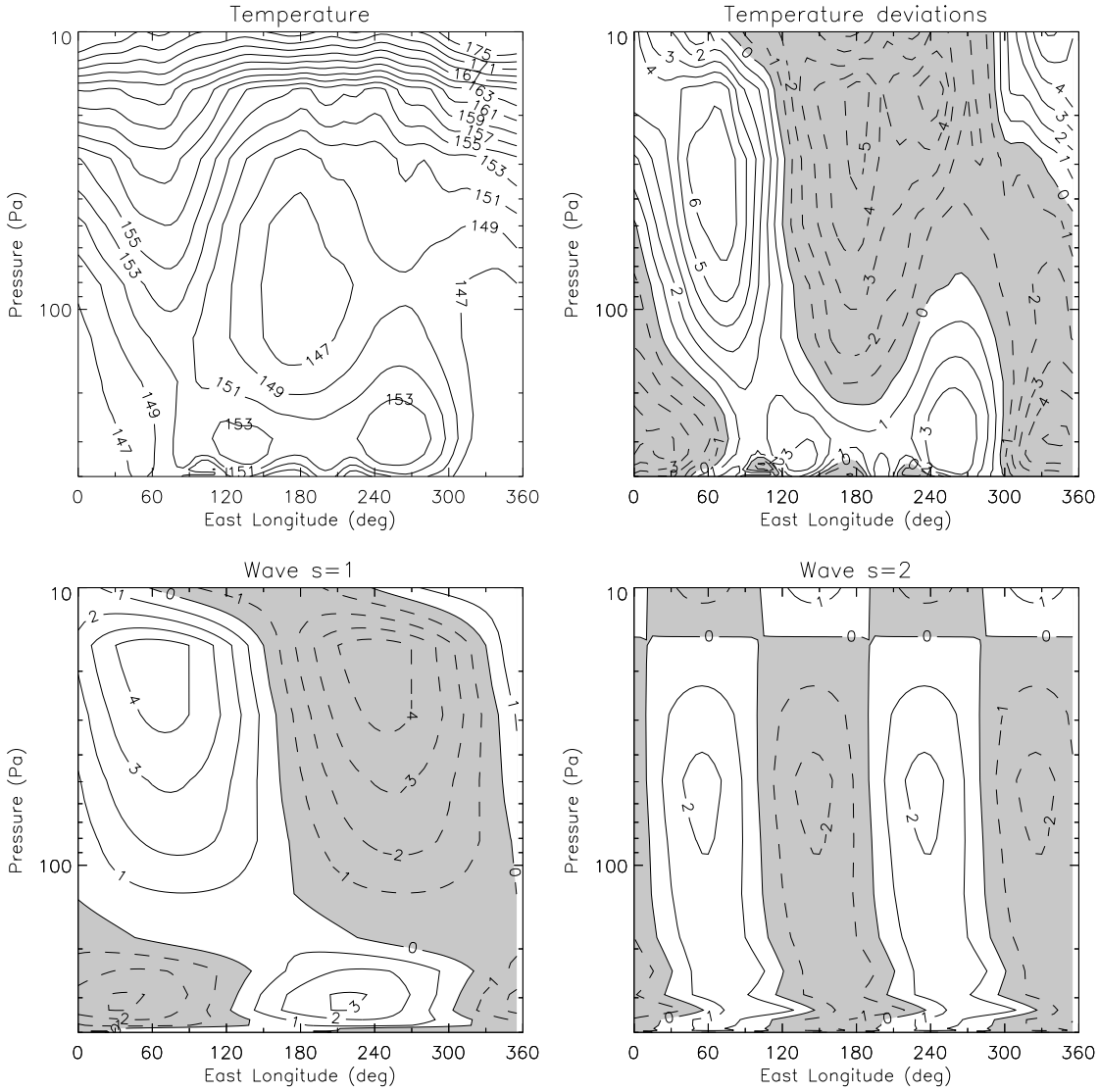

Figure 17: Montabone et al., Validation of MGS/TES data assimilation

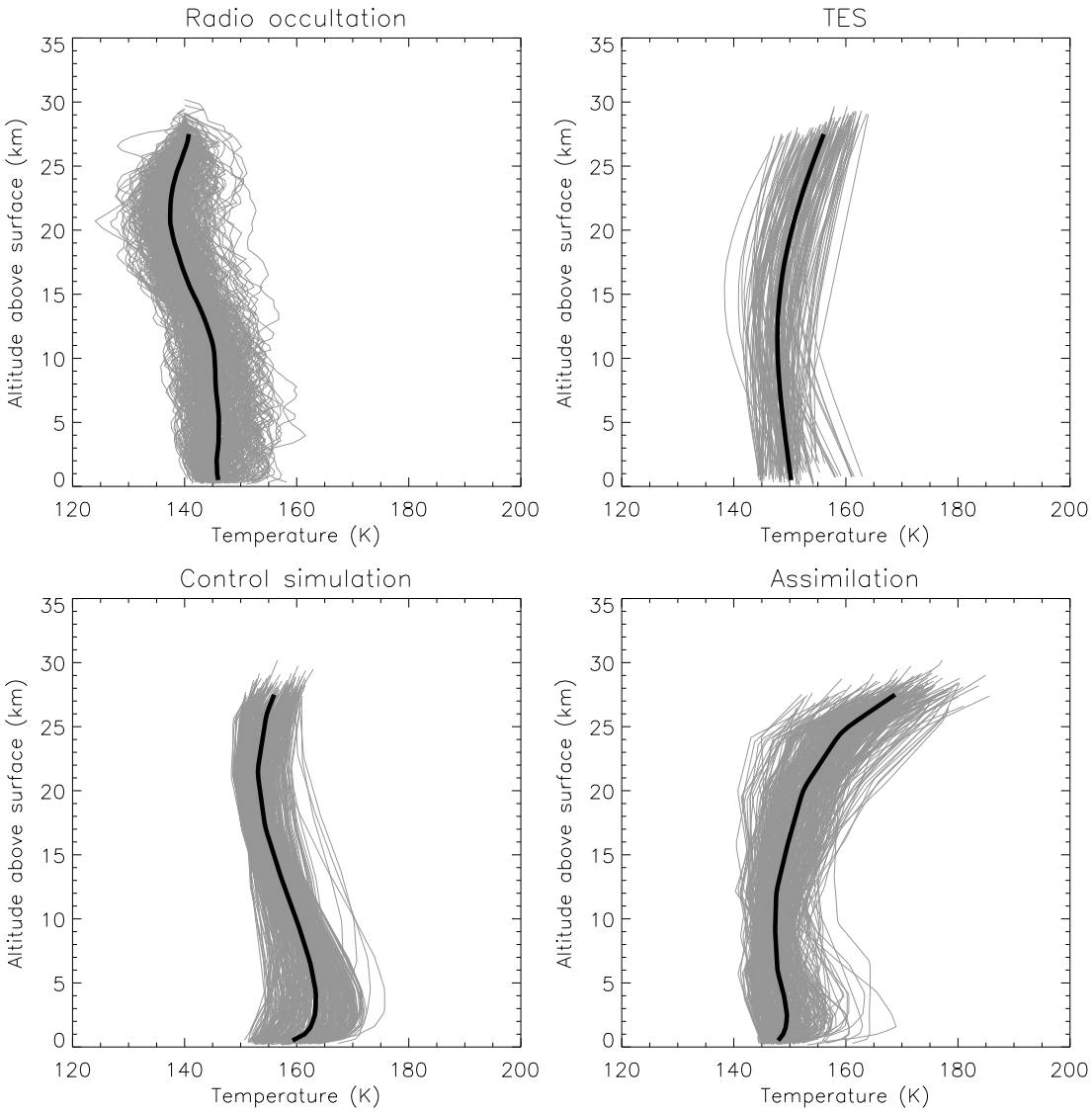

Figure 18: Montabone et al., Validation of MGS/TES data assimilation